THESIS APPROVAL

The abstract and thesis of Adam Jared Campbell for the Master of Science in Geology were presented April 9, 2009 and accepted by the thesis committee and the department.

COMMITTEE APPROVALS: Christina Hulbe

Christina L. Hulbe, Chair

K.M. Cruikshank

Kenneth M. Cruikshank

Aslam Khalil

M.A.K. Khalil

DEPARTMENT APPROVAL: Scott Burns

Scott F. Burns, Chair
Department of Geology

ABSTRACT

An abstract of the thesis of Adam Jared Campbell for the Master of Science in Geology presented April 9, 2009.

Title: Numerical Model investigation of Crane Glacier response to collapse of the Larsen B ice shelf, Antarctic Peninsula.

In March 2002, the Larsen B Ice Shelf disintegrated catastrophically. Many of the glaciers that fed the ice shelf are observed to have experienced increased rates of ice discharge and front retreat but the response is neither uniform nor universal. At one end of the range is the large response of Crane Glacier, which has sped up 3-fold from (~500 m a^{-1} to ~1500 m a^{-1}) in its downstream reach and by late 2006 thinned 150 meters since ice shelf collapse. Between March 2002 and early 2005, Crane Glacier's calving front retreated by about 11.5 km and is now oscillating about that position.

Here, the dynamic response of Crane Glacier to ice shelf collapse is investigated using a finite element model of momentum balance along a profile down the trunk of Crane Glacier. Assuming that the glacier was near equilibrium with its boundary conditions before ice shelf collapse, observed pre-collapse flow is used to tune the model. The model is then used to perform stress perturbation experiments to investigate the instantaneous response of the glacier to the removal of the ice shelf.

The response has two components, a minor dynamic change due to the stress perturbation as ocean and air replace the ice shelf at the downstream end of the glacier, and a large increase in the sliding speed, together with an increase in downstream stretching. The magnitude of the modeled instantaneous speedup has a 14% absolute difference to the observations and the instantaneous thinning rate associated with the change in downstream stretching is of the same order of magnitude as observations.

NUMERICAL MODEL INVESTIGATION OF CRANE GLACIER RESPONSE TO COLLAPSE OF THE LARSEN B ICE SHELF, ANTARCTIC PENINSULA

by

ADAM JARED CAMPBELL

A thesis submitted in partial fulfillment of the
requirements for the degree of

MASTER OF SCIENCE
in
GEOLOGY

Portland State University

2009

Dedication

I would like to dedicate this work to Jason H. Campbell (*December 1, 1970 – August 2, 2007*), my friend and brother.

For the planets gravitate around you,
and the stars shower down around you,
and the angels in heaven adore you,
and the saints all stand and applaud you.
so faraway,
so faraway and yet so close.

Acknowledgements

There are so many people that have contributed in my life and academic success that it is truly not possible to name them all. I would like to thank everyone who has helped me achieve this milestone, my family, my teachers, and my friends.

First I would like to thank my mother and father for raising me in a loving home and teaching me the importance of family. I have always relied on their love and support. I thank my brothers for being my best friends.

I would like to thank all my friends for supporting and encouraging me, especially my roommate Emily for encouraging me to stay enthusiastic and upbeat and Bill for always being there to drink beer and to provide a good distraction.

The students at The Portland State Geology Department are some of the most good natured I have ever met and, I really wouldn't have been able to graduate without the continuous support from my fellow students. Every teacher is the PSU geology department has helped with problems big and small throughout my time here and for that I thank them. Also, I would like to thank Nancy who helped me carefully navigate the minefield of PSU bureaucracy.

I would like to thank Jesse Johnson at the University of Montana for sharing important research notes and model files so that I could more easily learn to do glacier modeling.

I thank the members of my committee, Ken Cruikshank and Aslam Khalil for taking the time to review this work and helping me to improve it.

A huge debt of gratitude goes out to Olga Sergienko for constantly helping overcome the technical challenges of modeling and for providing so much direct help to this project. I have learned an incredible amount from her about ice physics and modeling. I don’t want to think about how long I would have been here if it was not for her.

Finally, I would like to thank my thesis supervisor, Christina Hulbe. Christina got me into this project from the its beginning. She has helped me to develop into a budding glaciologist. Her notes on my drafts have helped me to vastly improve my writing and her love of the subject matter constantly helped me to maintain enthusiasm.

This work was primarily supported by NASA grant NNG06GB42G and also by NSF grant ANT-0440670.

Table of Contents

List of Tables

List of Figures

Symbol Guide

Latin Letters

A	Glen flow rate factor		Pa^{-n} s^{-1}
$\overline{A}$	Mean Glen flow rate factor		Pa^{-n} s^{-1}
B_0	Flow rate factor	6.984×10^{-3}	Pa $s^{-1/n}$
C	Flow rate factor	0.16612	[unitless]
C_p	Heat capacity of ice	2093	J K^{-1} kg^{-1}
E_{xx}	Stress transformation variable		Pa
E_{xz}	Stress transformation variable		Pa
E_{zz}	Stress transformation variable		Pa
G	Geothermal heat flux		K m^{-1}
H	Ice thickness		m
$\mathbf{I}$	Identity matrix		[unitless]
K	Flow rate exponent	1.17	[unitless]
L	Horizontal length of domain		m
Q	Activation energy for creep	7.88×10^{4}	J mol^{-1}
R	Universal gas constant	8.314	J mol^{-1} K^{-1}
S	Upper surface elevation		m
SS	Sum of squares		[unitless]
W	Sum of squares error factor		m^2 s^{-2}

$\dot{a}$	Upper surface mass balance		m s^{-1}
a_x	Coordinate transformation constant		m^{-1}
b_n	Constant upper surface mass balance		m s^{-1}
g	Gravitational acceleration	9.81	m s^{-2}
$\mathbf{g}$	Gravitational acceleration vector		m s^{-2}
h_w	Water level elevation		m
k	Sliding law rate factor		m s^{-1} Pa^{1-q}
l	Flightline distance		m
m	Flow enhancement factor	1	[unitless]
n	The Glen flow law exponent	3	[unitless]
$\hat{n}$	Outward pointing unit vector		[unitless]
p	Pressure		Pa
p_{bs}	Backstress pressure		Pa
p_e	Effective pressure		Pa
p_i	Ice overburden pressure		Pa
p_w	Water pressure		Pa
q	Sliding law exponent	3	[unitless]

r	Sum of squares velocity difference		$m^2\ s^{-2}$
t	Time		s
u	Horizontal component of velocity vector		$m\ s^{-1}$
$\mathbf{u}$	Velocity vector		$m\ s^{-1}$
u_b	Horizontal component of basal velocity vector		$m\ s^{-1}$
u_s	Horizontal component of velocity of the upper surface of glacier		$m\ s^{-1}$
w	Vertical component of velocity vector		$m\ s^{-1}$
w_b	Vertical component of basal velocity vector		$m\ s^{-1}$
w_s	Vertical component of velocity of the upper surface of glacier		$m\ s^{-1}$
w_x	Water level slope		[unitless]
x	Horizontal component of position vector, increasing upstream		m
x'	Scaled horizontal coordinate		m
z	Vertical component of position vector, increasing upward		m
z_0	Sea level elevation		m

Greek Letters

β	Coefficient of pressure dependence on melting of water		$K\ Pa^{-1}$
Δwl	Height of water column at upstream end		m
$\dot{\boldsymbol{\varepsilon}}$	Strain rate tensor		s^{-1}
$\dot{\varepsilon}_0$	Minimum strain rate	1×10^{-30}	s^{-1}
η	Viscosity		Pa s
θ	Temperature of ice		K
θ^*	Pressure adjusted temperature of ice		K
θ_r	Triple point temperature of water	273.15	K
θ_s	Surface temperature of ice		K
κ	Thermal diffusivity of ice	2.1	$W\ m^{-1}\ K^{-1}$
ξ	Scaled vertical coordinate		[unitless]
ξ_0	Temperature profile variable		m^{-1}
ρ_i	Density of ice	910	$kg\ m^{-3}$
ρ_{sw}	Density of seawater	930	$kg\ m^{-3}$
ρ_w	Density of freshwater	1000	$kg\ m^{-3}$
σ_v	Error in velocity observation		$m\ s^{-1}$
$\boldsymbol{\sigma}$	Stress tensor		Pa
$\boldsymbol{\sigma}'$	Deviatoric stress tensor		Pa
τ_b	Basal shear stress		Pa
τ_d	Driving stress		Pa

1 Introduction

West Antarctica is one of the fastest warming regions on Earth and its coastal glaciers and ice shelves are responding to that warming. Since 1957, the Antarctic Peninsula (AP) has experienced air temperature warming at a rate of 0.11 ± 0.06 ºC per decade (Steig et al., 2009). Simultaneously, ice shelves and outlet glaciers have thinned and retreated (Cook et al., 2005; Scambos et al., 2000). Several ice shelves in the northern AP have disintegrated suddenly in response to warming. The largest of these events was the disintegration of the Larsen B ice shelf on the eastern side of the peninsula (Figure 1.1) in the late austral summer of 2002 (Scambos et al., 2003). The event exposed the glaciers that had previously flowed into the ice shelf to the ocean, transforming them instantaneously into tidewater glaciers.

Glaciers with grounded marine termini are referred to as tidewater glaciers. These glaciers have a calving front at their downstream end where icebergs form and float away from the glacier. The calving front may be at the grounding line or, the downstream end of the glacier may go afloat in the water and develop a floating ice tongue (Benn and Evans, 1998).

Several of the glaciers that fed the Larsen B ice shelf have responded to the ice shelf collapse by accelerating, thinning and retreating at the downstream end (Hulbe et al., 2008; Rignot et al., 2004; Scambos et al., 2004). Understanding the mechanisms by which grounded glaciers react to the disintegration of a terminal ice shelf is of interest because of the potential for rapid input to sea level as glaciers adjust to the change in downstream boundary condition. The ice on the AP is equivalent to 0.5 m of sea level rise but, the processes at work here are relevant to larger reservoirs of ice elsewhere (Bamber et al., 2009; Payne et al., 2004; Thomas et al., 2004).

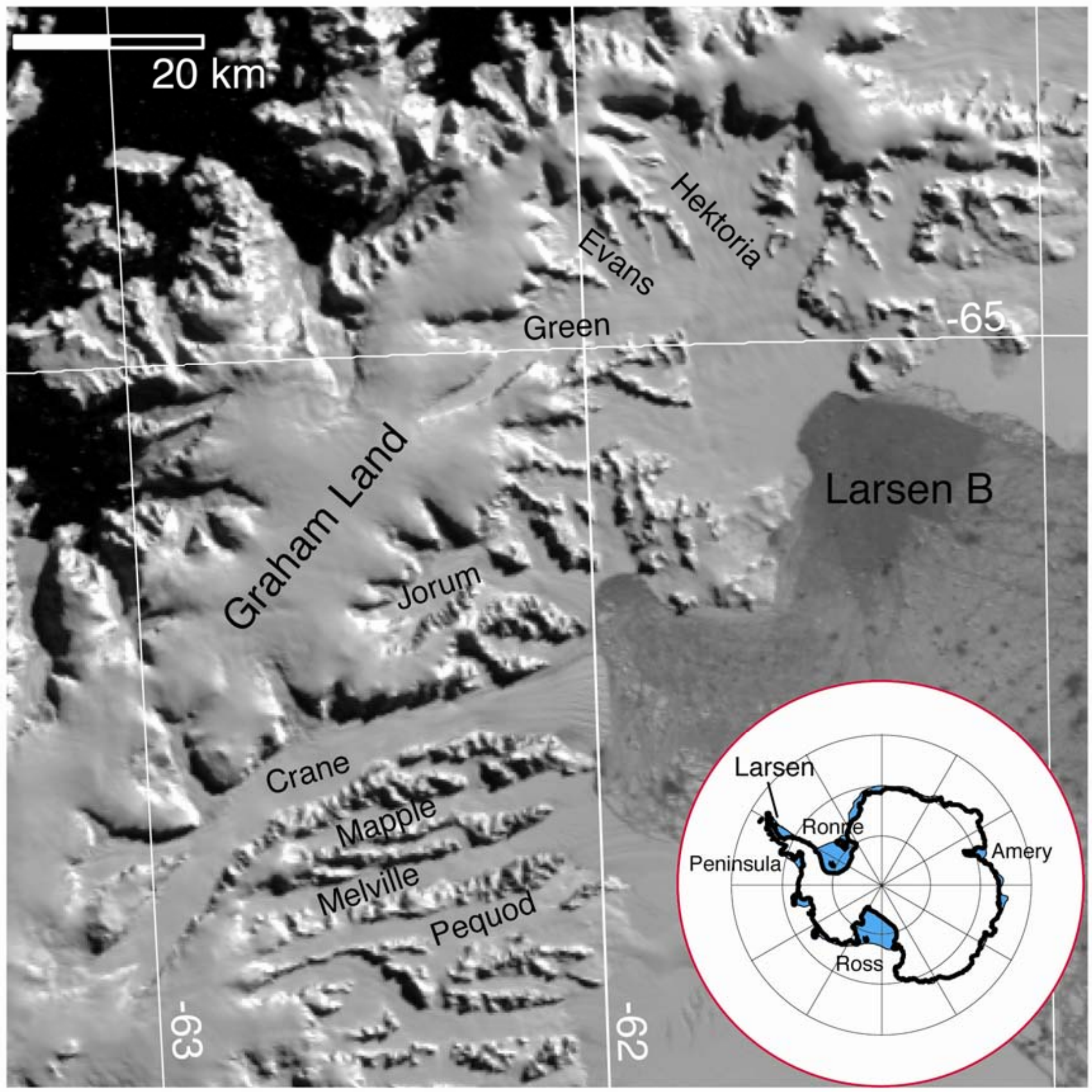

Figure 1.1 Crane Glacier is located on the eastern side of the Antarctic Peninsula. MODIS image from 17 March 2002 provided by the National Snow and Ice Data Center, Boulder, Colorado, USA.

The response of the Larsen B glaciers to ice shelf collapse has been varied with some glaciers experiencing a prolonged retreat and thinning and others reaching a stable post-collapse front position and ice-thickness relatively quickly. Valley geometry is presumed to play an important role in guiding the reaction of glaciers to ice shelf disintegration, through its effect on glacier flow or a calving instability (Section 1.2).

1.1 Antarctic Peninsula and Climate

The mountain chain forming the AP is heavily glaciated. Plateau ice caps drain into mountain glaciers that flow toward either the Bellingshausen Sea on the west or the Weddell Sea on the east. This mountain chain has a more maritime climate than the polar continental climate of the Antarctic interior with an average precipitation rate of 0.87 m a^{-1} water equivalent (w.e.) as compared to 0.14 w.e. m a^{-1} on the continental interior. The AP receives 18% of the continent’s snowfall despite occupying only 3% of the land area. The mean annual air temperature on the eastern side of the AP typically ranges from -5 ºC to -17 ºC, about 3 to 5 ºC cooler than the western side (Pritchard, 2007).

During the Last Glacial Maximum (LGM), ice expanded into middle and outer submarine shelves surrounding the AP. Post-LGM deglaciation occurred relatively slowly, mainly between >14 and 6 ka before present (BP). A climatic maximum occurred around 4 to 3 ka BP followed by a gradual cooling (Ingolfsson and Hjort, 2002). There is evidence for the Larsen B ice shelf to have existed continuously since its formation 10.5 ka BP (Pritchard, 2007).

1.2 Reaction of Crane Glacier to Ice Shelf disintegration

Changing climate around the AP has resulted in the disintegration of several ice shelves. The largest such disintegration was of the Larsen B ice shelf in March 2002, during the austral summer (Scambos et al., 2003). Subsequent to the collapse of the Larsen B ice shelf, Crane Glacier experienced a prolonged retreat and thinning (Scambos et al., 2004). In 2005, the front position of Crane Glacier began to hold a steady position.

Crane Glacier's reaction to the disintegration of the Larsen B may be attributed to one (or both) of two changes. First, when Larsen B collapsed, Crane Glacier instantaneously became a tidewater glacier that is susceptible to a calving instability at its downstream end. Second, Crane Glacier also experienced an abrupt change in its downstream stress boundary condition when the ice shelf was replaced with water and air.

1.3 Problem Statement

The reaction of Crane Glacier to the rapid disintegration of the Larsen B ice shelf is likely the result of two mechanisms, the stress perturbation at the downstream end of the glacier and the calving effects associated with the instantaneous transition to a calving glacier without a floating ice tongue at its terminus. This study will investigate this transition using observational data and a numerical model of glacier flow. An experiment is designed to investigate glacier response to ice shelf collapse. The results of this experiment are compared with observed changes in glacier flow.

A numerical model is developed for the present work. This model uses glacier surface and bed elevation obtained from airborne radar surveys around the Antarctic Peninsula. A Glen flow law rheology is used together with an estimate of internal temperature (Hooke, 2005). A sliding law driven by basal water pressure is used and is tuned to reproduce observed velocities along the flightline prior to ice shelf collapse. The 2-D momentum balance along the flightline is solved using a finite element model.

2 Observations

2.1 Profile Geometry of Crane Glacier

Glacier surface and bed elevation were measured along a flight over many AP ice caps and outlet glaciers made in November 2002 by NASA Wallops Flight Facility, The University of Kansas, the Chilean Centro de Estudios Científicos (NASA/KU/CECS). Airborne laser, radar and GPS were used to conduct the survey. The raw observation interval along the ground track varies between about 100 and 200 meters. The data were obtained via personal communication (Thomas, 2005) (Figure 2.1). This data set is neither complete nor along the centerline of the glacier. It is, nevertheless, the most accurate and highest resolution view of glacier surface and bed geometry available.

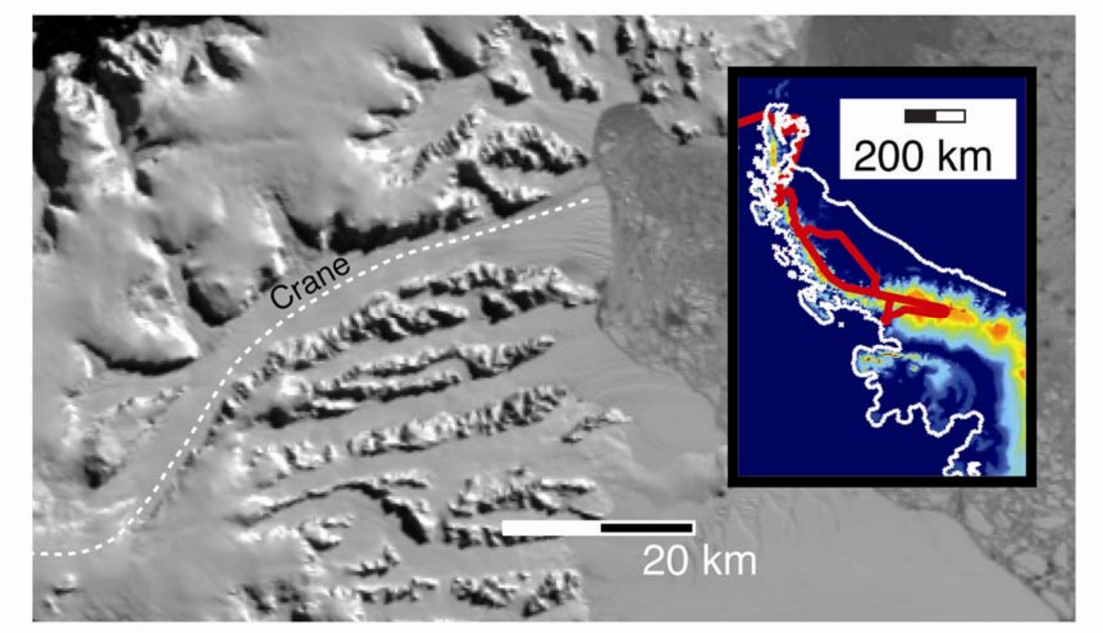

Figure 2.1 Flightline over Crane Glacier from NASA/KU/CECS team plotted on MODIS image from 17 March 2002.

A subset of the complete NASA/KU/CECS data set, approximately 80 km along Crane Glacier, is used here. The data are interpolated to a regular spacing of 100 m (Figure 2.2). There is a large bedrock high located about 20 km upstream of the glacier terminus at the time of the flight, the region downstream of this is henceforth referred to as the downstream reach and the region upstream is referred to as the upstream reach of the glacier.

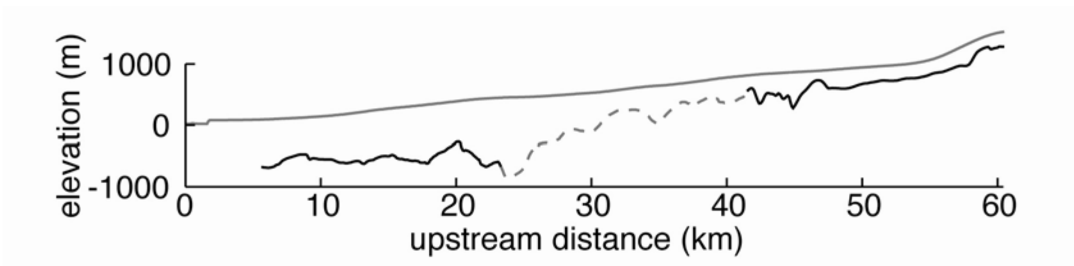

Figure 2.2 Laser and radar reflections were used to determine upper surface (grey) and bed elevations (black). Where no data exists for bed elevations (dashed grey), an interpolation scheme is used to provide an estimate. The estimate is conducted by inverting the surface-speed equation for ice thickness is a first-order flow law

Bed elevation is missing along part of the Crane Glacier profile due to reduced radar return strength. The cause is not known but assumed to be heavy crevassing (personal communication Thomas, 2005). The data gap is filled in here by inverting observed glacier surface velocity and elevation for ice thickness. The missing bed elevation is needed for the modeling effort. Assuming the driving stress τ_d is balanced by basal drag, an expression can be written for surface speed along a flow line:

$$u_s = \frac{2\overline{A}H}{n+1}\tau_d^n \tag{2.1}$$

in which, $\overline{A}$ represents a mean flow-law rate factor, H represents ice thickness, and n represents the flow-law exponent (Van der Veen, 1999). The gravitational driving stress is defined

$$\tau_d = \rho_i g H \frac{dS}{dl} \tag{2.2}$$

in which, S represents the surface elevation, l represents the flightline following coordinate, g represents gravitational acceleration, and ρ_i represents the column-average ice density. With this the expression for the surface velocity becomes

$$u_s = \frac{2\overline{A}H}{n+1}(\rho_i g H \frac{dS}{dl})^n \tag{2.3}$$

where it is commonly assumed that n is 3. Equation 2.3 does not account for sliding of ice along the base of the glacier. The flow-law rate factor $\overline{A}$, is tuned to fit the observed values of H and u_s both upstream and downstream of the data gap and Equation 2.3 is rearranged to solve for H.

The flightline surface and bed elevation dataset is not ideal because it is not along the centerline of the glacier. Proximity to the valley sidewall may affect the radar return via reflections from the sidewall. The flightline veers northward from the centerline of the glacier along its downstream reach (Figure 2.1). Reflections from the sidewall may result an in underestimate of the basal elevation.

2.2 Bathymetry of Crane Outlet

Following collapse of the Larsen B ice shelf, bathymetry in the embayment was measured using multibeam sonar (Figure 2.3, Domack et al., 2006). These data can be used to provide context for the NASA/KU/CECS flightline. The bathymetry data indicates a rough bed with steps (shoals) oriented across-valley. This is consistent with the downstream section of the basal elevation data from the flightline. It is unknown if the cross-valley shoals are till deposits or bedrock.

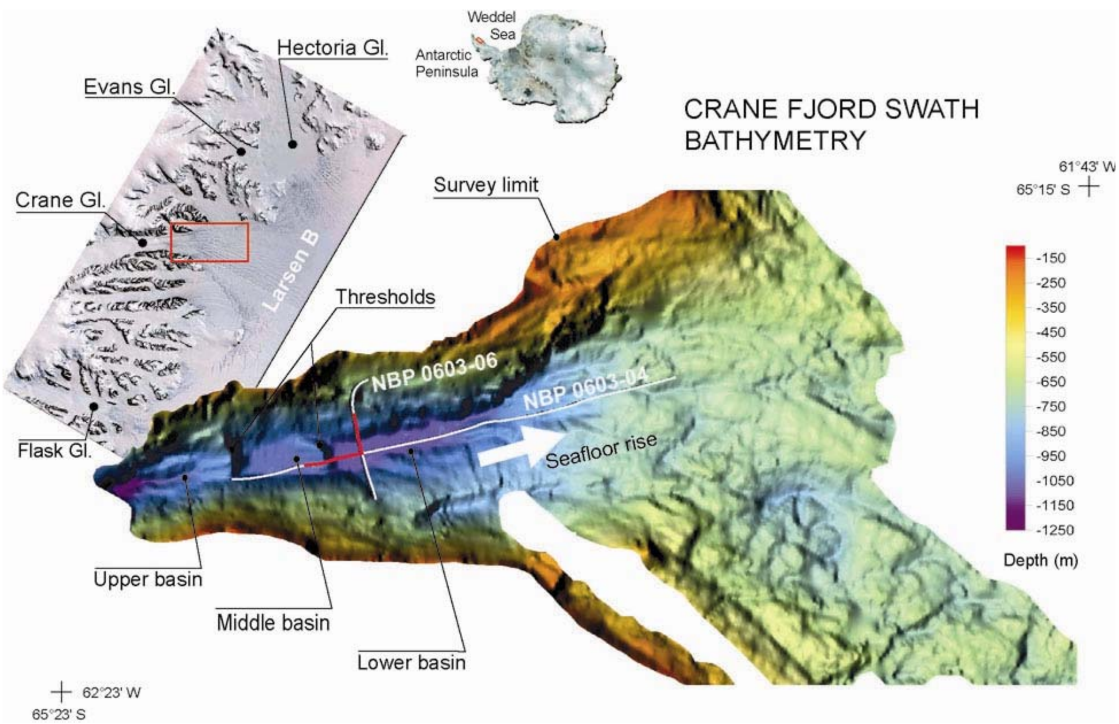

Figure 2.3 Bathymetry data of the Crane Glacier outlet (Domack et al., 2006) shows a series of shoals.

2.3 Surface Velocity

Surface velocity has been determined over several intervals using an image-to-image correlation technique and visible-band data from two space-born sensors (Hulbe et al., 2008; Lamb, 2006; Scambos et al., 2004). Advanced Spaceborne Thermal

Emission and Reflection Radiometer (ASTER) and Landsat 7 image pairs were used. The time intervals of velocity observations are: from 27 January 2000 to 06 December 2001, from 06 December 2001 to 18 December 2002, from 18 December 2002 to 20 February 2003, from 18 December 2002 to 13 January 2004, from 13 January 2004 to 27 September 2004, and from 24 November 2005 to 25 November 2006. The method tracks surface features in related images over time yielding an average displacement over the time period separating the images. Surface velocity is then calculated according to the displacement distance and direction. Surface speed is interpolated onto the Crane Glacier flightline using a search radius of 500 m. Errors in the velocities depend on the resolution of imagery and on the time interval between images (NSIDC, 2009).

The velocity data are discontinuous in both time and space. This limitation is due to persistent cloud cover in the region. The result is that our view of glacier response to ice shelf collapse is not complete.

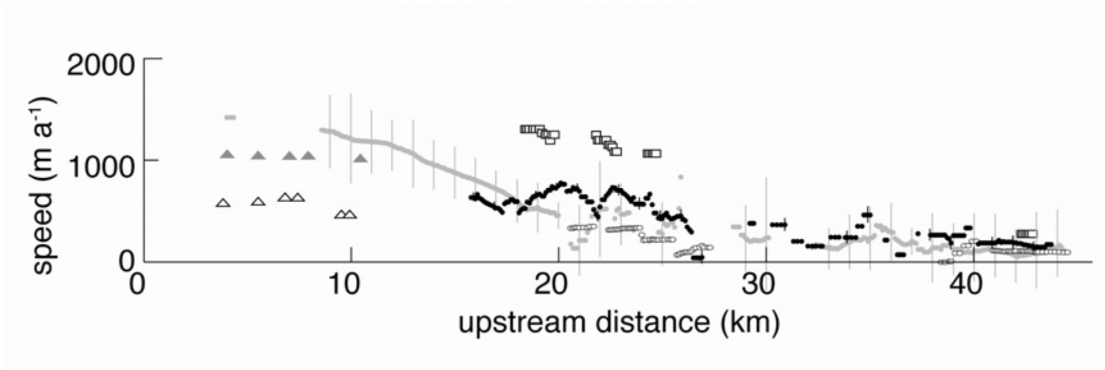

Figure 2.4 Surface velocities interpolated onto the flightline for time periods: from 27 January 2000 to 06 December 2001 (hollow triangles), from 06 December 2001 to 18 December 2002 (filled triangles), from 18 December 2002 to 20 February 2003 (filled grey circles), from 18 December 2002 to 13 January 2004 (filled black circles), from 13 January 2004 to 27 September 2004 (hollow circles) and, from 24 November 2005 to 25 November 2006 (hollow squares). Surface velocities experience a large speed up at the downstream end immediately subsequent to ice shelf disintegration. Velocities at the upstream reaches of Crane Glacier do not appear to have changed following ice shelf disintegration.

Two distinct regions of the glacier emerge in the post-collapse velocity. In the upstream reach (Figure 2.4), surface speed is spatially variable, tracking variations in ice thickness and surface slope. In the downstream reach, speed increases continually toward the glacier front. The transition is in the vicinity of a bedrock high. The change in flow pattern indicates either a spatial change in the basal boundary condition, a response to the change in boundary condition at the downstream end of the glacier, or some combination of the two.

Following the collapse of Larsen B, the speed of Crane Glacier increased, decreased, and then increased again. The glacier front retreated considerably during this interval, complicating interpretation of the flow speed changes. Before the collapse of Larsen B, surface speed along the entire glacier was spatially variable in the manner of its upstream reach (Rignot et al., 2004; Scambos et al., 2004). The time-varying glacier speeds may be due to upstream propagation of the stress perturbation at the downstream end via longitudinal stresses and changes in ice thickness and surface slope or perhaps to changes in glacier sliding.

2.4 Glacier Front Position

Glacier front positions are mapped using Moderate Resolution Imaging Spectroradiometer (MODIS) level 1B visible-band images archived at the National Snow and Ice Data Center. Front positions are digitized by hand, at the transition area between the relatively bright upper surface of the glacier and the shadow cast by the calving front. These front positions are interpolated onto the NASA/KU/CECS flightline as a means of comparing the relative front positions with other data sets. The pixel size is 250m for the images so digitization error in the front position is of the same size (Figure 2.5).

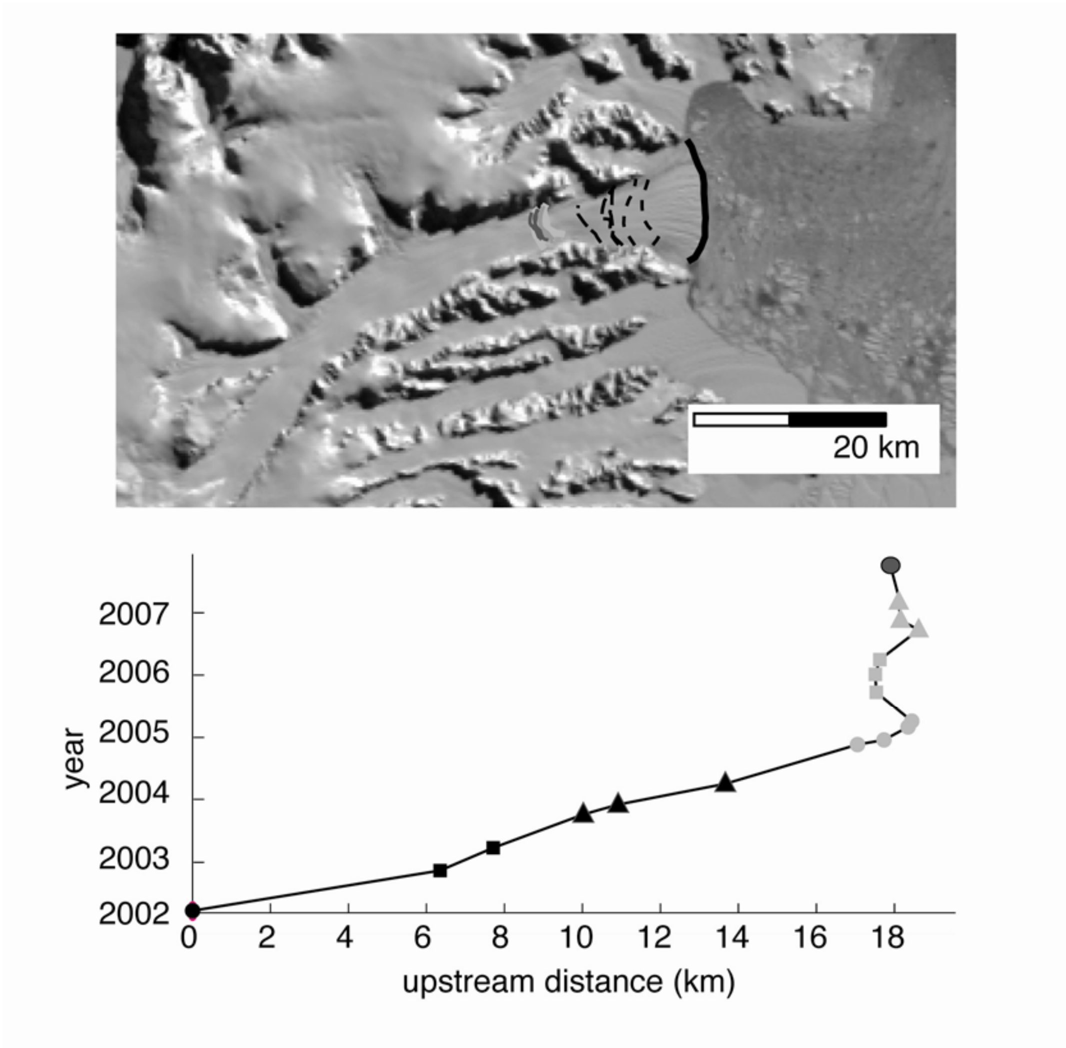

Figure 2.5 The front of Crane Glacier retreated rapidly up until 2005 when it experienced a slight advance and subsequent stability. Front positions are plotted on top of a MODIS image taken immediately after ice shelf disintegration on 17 March 2002(upper) for summer seasons: 2001-02 (black line), 2002-03 (short dashed black line), 2003-04 (long dashed black line), 2004-05 (light grey), 2005-06 (medium grey) and, 2006-07 (dark grey). Front positions are interpolated onto the flightline with respect to front position immediately after ice shelf disintegration over time (lower) for summer seasons: 2001-02 (black circles), 2002-03 (black squares), 2003-04 (black triangles), 2004-05 (light grey circles), 2005-06 (light grey squares), 2006-07 (light grey triangles) and, 2007-08 (dark grey circle).

Front positions for Crane Glacier were digitized using all available cloud-free MODIS images acquired after ice shelf collapse. A subset of these data with relatively uniform spacing (late spring and late summer/early fall) are presented and used here.

The dates are: 17 March 2002, 27 November 2002, 20 March 2003, 02 October 2003, 30 March 2004, 15 November 2004, 13 December 2004, 28 February 2005, 03 April 2005, 22 September 2005, 05 January 2006, 01 April 2006, 19 September 2006, 24 September 2006, 18 November 2006, 07 January 2007, and 05 March 2007.

Subsequent to the disintegration of the Larsen B ice shelf, Crane Glacier retreated rapidly until 2005. The front position has remained relatively stable since 2005 with minor oscillations about that position.

2.5 Repeat Ice Surface Elevation

Surface elevation is observed by the Geoscience Laser Altimeter System (GLAS) on NASA's Ice, Cloud, and Land Elevation Satellite (ICESat). Observations along a track suitable for interannual comparison run roughly perpendicular to glacier flow are available for 23 October 2003, 10 October 2004, 28 October 2005, and 31 October 2006. The data used here were acquired along satellite track 0018 with laser 2A in 2003, 3A in 2004, 3D in 2005, and 3G in 2006. The spacing of spot measurements acquired by GLAS is 172 m having an effective spot size of 70 m (Shuman et al., 2008). The errors in the derived surface elevation are ±0.2 m under clear sky conditions and up to about 2 m under thin cloud cover (Zwally et al., 2002). These observations provide a separate measure of ice surface elevation from the data acquired by the NASA/KU/CECS flightline. This data provide insight into the transient response of the glacier to ice shelf collapse (Figure 2.6).

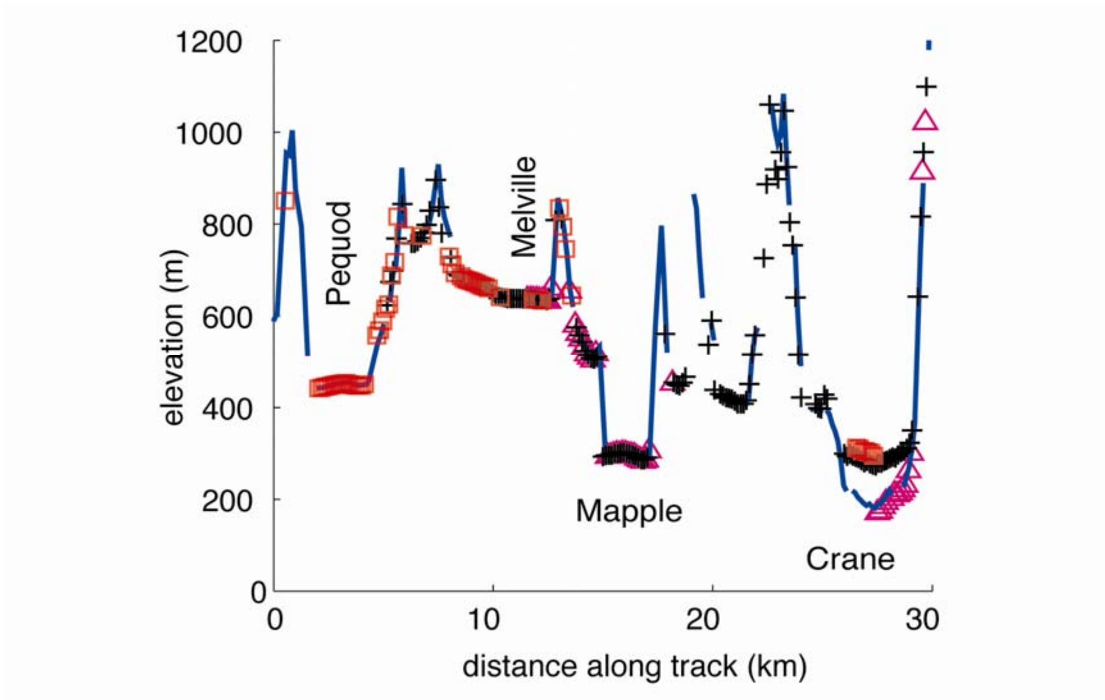

Figure 2.6 Elevation data along laser tracks from GLAS system on ICESat satellite from dates: 23 October 2003 (hollow squares), 10 October 2004 (crosses), 28 October 2005 (lines), and 31 October 2006(triangles). The pattern indicates that Crane Glacier rapidly thinned in 2005

2.6 Climatic Observations

Climate data near the former Larsen B ice shelf is limited, with only a few observation sites in the region. The mean annual air temperature is about -9 ºC near the downstream end of Crane Glacier (Vaughan and Doake, 1996). The altitudinal lapse rate is -0.0044 ºC m^{-1} in the eastern AP region (Morris and Vaughan, 2003). A regional climate model has been used to compute surface precipitation minus sublimation (van Lipzig et al., 2004). The model yields precipitation minus sublimation ranging from 500 to 2000 mm w.e. a^{-1} in the region of the Crane Glacier flightline.

3 Methods

3.1 Numerical Model

A 2-D flowline model is developed to explore the reaction of Crane Glacier to changes in boundary conditions. The model uses a finite element method to solve momentum conservation equations for glacier ice using observed bed geometry and boundary conditions appropriate for the glacier. For this study the commercially available COMSOL Multiphysics™ software package is used to generate the model mesh and solve the governing equations.

The solver software uses Lagrange quadratic elements that allow the second derivative of velocity to be computed accurately (Johnson and Staiger, 2007). Nonlinear systems are solved using the modified Newton iterative solver (Deuflhard, 1974). The linear system of equations are then solved by the UMFPACK linear solver (Davis, 2004).

3.1.1 Finite Element Methods

The finite element method (FEM) is a numerical method used to approximate the solutions to partial differential equations (PDEs). The equations are solved on a set of points (“nodes”) that together define a mesh that represents the model domain. FEM is a numerical integration instead of an approximation of the derivative terms in the PDE as is done in finite difference modeling. The FEM approach is well suited to complicated geometries such as the bed of Crane Glacier because it does not require a regular mesh geometry.

3.1.2 Model Domains and Meshes

When designing a model domain several competing factors must be considered, such as numerical stability, computation time, and interest in capturing details of glacier behavior in specific areas of the model domain. Several different geometries are used in the present work. The meshes used to solve each of these are described with the geometry.

A persistent problem encountered during model design and testing was numerical noise due to large gradients in the elevation. This noise sometimes prevented convergence of the numerical solution. This was handled by smoothing the elevation and by reducing the upstream extent of the model domain. In one particular instance a large gradient bed elevation over a short distance resulted in non-convergence for the model. This area was smoothed by removing the offending basal elevation points and using a linear slope derived from neighboring points.

The momentum equation is diagnostic, a specified surface elevation and ice thickness fields are used to compute an accompanying velocity field, while the mass conversation equation is prognostic and may predict a changing thickness field. Model development began with momentum balance, using a non-scaled coordinate system (Figure 3.1). Time-transient solutions involve changing ice thickness, and perhaps changing glacier length. This is most easily handled via a scaled coordinate system (Figure 3.2). The scaled coordinate system used in some of the models, scales the vertical coordinate of the glacier such that the upper surface is represented by a value of 1 on the vertical axis and the basal surface is represented by a value of 0, while the horizontal coordinate is not transformed. Time-transient experiments are not addressed in the present effort however the model is built in such a way that time-transient experiments could eventually be developed.

The 2-D mesh used to solve for conservation of momentum PDEs in non-scaled coordinate systems is used in experiments to estimate the deformation velocity of Crane Glacier and solving for the Glen flow law (Figure 3.1).

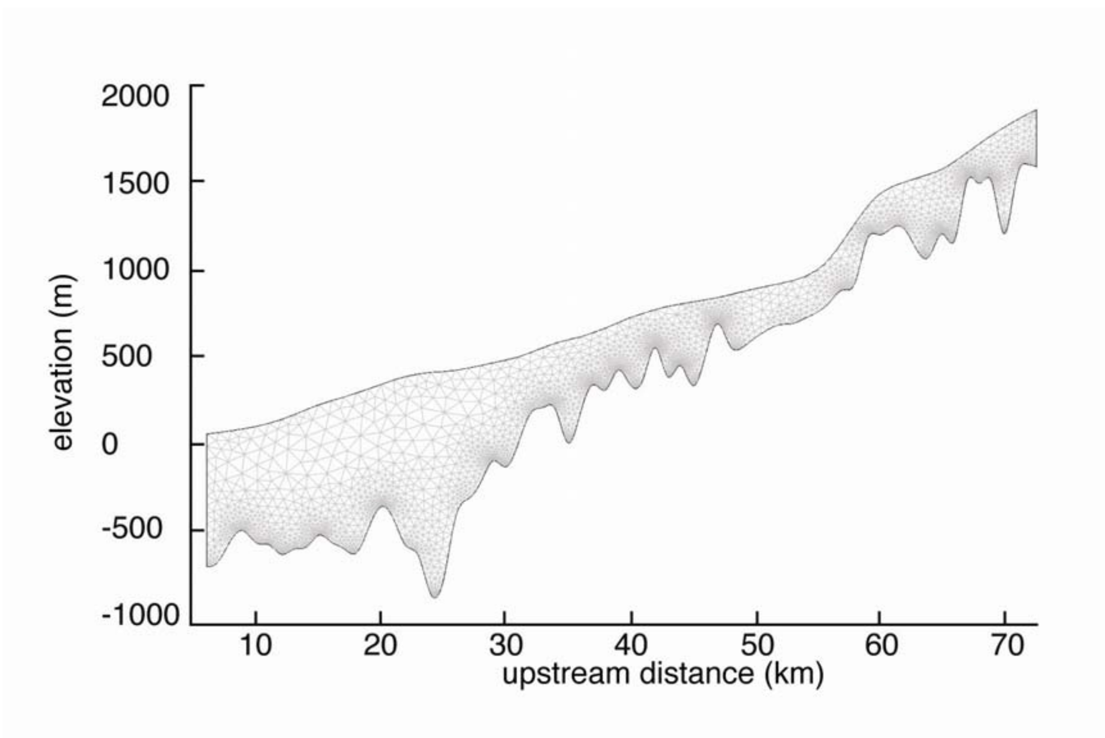

Figure 3.1 Mesh for the non-scaled models consists of 11501 nodes with an increase density near large gradients in the glacial geometry.

Table 3.1 Mesh statistics for non-scaled mesh.

Quantity	Value
Number of Elements	11501
Minimum element quality	0.0446
Element area ratio	8.85×10^{-5}

The 2-D mesh used to solve conservation of mass and momentum PDEs in scaled coordinates systems is used in experiments estimating the combined sliding and deformation velocity of Crane Glacier (Figure 3.2). These model domains are limited to the downstream reach of Crane Glacier in order to avoid numerical instabilities introduced by large gradients in basal elevation in the upstream reach.

Table 3.2 Mesh statistics for scaled mesh in mass and momentum conservation mode.

Quantity	Value
Number of Elements	26250
Minimum element quality	0.0010
Element area ratio	1.0000

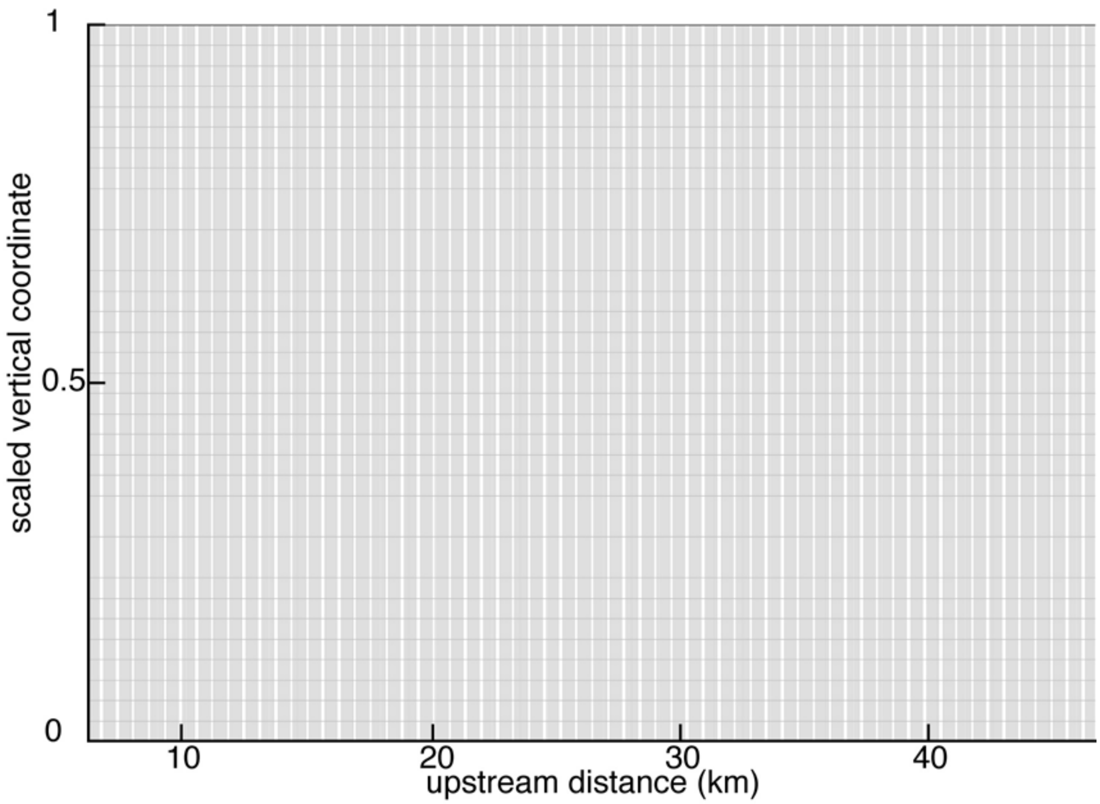

Figure 3.2 Rectangular mesh for scaled equations has 751 horizontal and 36 vertical grid nodes.

Perturbation experiments are conducted using a model domain limited to the lower elevation part of the glacier. The downstream end of the domain is at the post-ice shelf collapse glacier front location. The upstream end of the domain is placed far enough upstream to be unaffected by shelf collapse (as observed; see Section 2.3). The limited domain allows higher resolution in regions of interest than would otherwise be possible and avoids problems related to numerical noise (Figure 3.3).

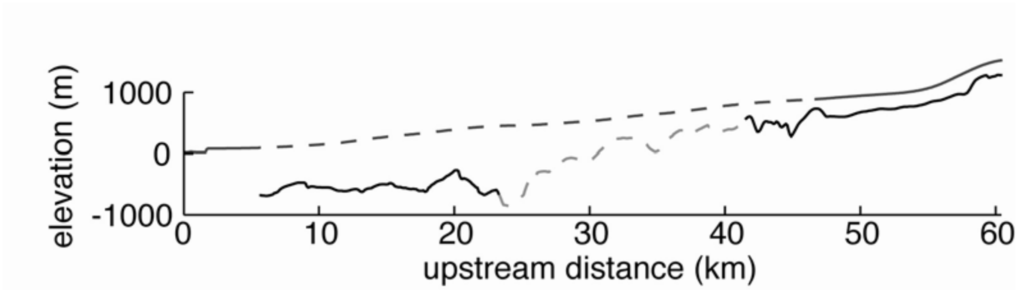

Figure 3.3 A subset of the geometry provided by the NASA/KU/CECS flightline data, indicated by dashed line on glacier surface, were used in the model in order to increase resolution in the downstream area of interest.

The numerical solver uses an iterative approach to find a solution to the governing equations. At the end of each iterative step, solutions to the current and prior steps are compared until the absolute difference between the current solution and previous solution falls below a prescribed cutoff, that is, the solution converges. For this study convergence is set at 1×10^{-6}. In some circumstances, high frequency errors accumulate and the solution cannot converge. Such instability may be handled either numerically or by modification of the model geometry.

3.2 Conservation Equations for Mass and Momentum and Boundary Conditions

3.2.1 Conservation Equations

The evolution of a glacier may be described using a set of conservation equations for momentum, mass, and energy - along with appropriate boundary conditions and material properties (Van der Veen, 1999). In the present work, the first two are considered while ice temperature is held fixed (see Section 3.4.1), they are:

$$\nabla \cdot \mathbf{u} = 0 \tag{3.1}$$

$$\frac{d\mathbf{u}}{dt} = \nabla \cdot \boldsymbol{\sigma} + \rho_i \mathbf{g} \tag{3.2}$$

The 2-D analysis is restricted to the *xz* plane, referred to as a flowline, which is described by the unit vector $\hat{i}$ in the x direction and $\hat{k}$ in the z direction. The velocity vector is represented by: $\mathbf{u} = u\hat{i} + w\hat{k}$, $\mathbf{g} = -g\hat{k}$, and $\boldsymbol{\sigma}$ represents the stress tensor. Total time derivatives are expressed with $\frac{d}{dt}$ and partial space derivatives with $\nabla = \frac{\partial}{\partial x}\hat{i} + \frac{\partial}{\partial z}\hat{k}$. The assumption is made that this flowline is on the centerline of the glacier and the effects of lateral drag by the valley sidewalls can thus be ignored.

The stress-strain relationship for the ice is

$$\boldsymbol{\sigma}'_{ij} = 2\eta\dot{\boldsymbol{\varepsilon}}_{ij} \tag{3.3}$$

where η represents a nonlinear viscosity and, σ'_{ij} represents the *ij* element of the deviatoric stress tensor,

$$\boldsymbol{\sigma}'_{ij} = \boldsymbol{\sigma}_{ij} - p \tag{3.4}$$

in which, p represents pressure. The corresponding element of the strain rate tensor $\dot{\varepsilon}_{ij}$ has the form

$$\begin{pmatrix} \dot{\varepsilon}_{xx} & \dot{\varepsilon}_{xz} \\ \dot{\varepsilon}_{zx} & \dot{\varepsilon}_{zz} \end{pmatrix} = \begin{pmatrix} \dfrac{\partial u}{\partial x} & \dfrac{1}{2}\left(\dfrac{\partial u}{\partial z} + \dfrac{\partial w}{\partial x}\right) \\ \dfrac{1}{2}\left(\dfrac{\partial u}{\partial z} + \dfrac{\partial w}{\partial x}\right) & \dfrac{\partial w}{\partial z} \end{pmatrix} \tag{3.5}$$

Glacier ice is a non-Newtonian fluid having a rheology defined using the Glen flow law (Glen, 1955). The flow law has the form

$$\eta = \frac{1}{2} A(\theta^*)^{-1/n} (\dot{\boldsymbol{\varepsilon}} + \dot{\varepsilon}_0)^{(1-n)/n} \tag{3.6}$$

in which the second invariant of the strain rate tensor

$$\dot{\boldsymbol{\varepsilon}}^2 = \nabla \mathbf{u} + (\nabla \mathbf{u})^T = \frac{1}{2} \sum_{ij} \dot{\boldsymbol{\varepsilon}}_{ij} \dot{\boldsymbol{\varepsilon}}_{ij} \tag{3.7}$$

is used. $\dot{\varepsilon}_0$ is a small number ($\dot{\boldsymbol{\varepsilon}} >> \dot{\varepsilon}_0$) introduced to prevent a negative viscosity in the initial stages of the numerical solution. The temperature dependent flow law rate factor $A(\theta^*)$ is defined

$$A(\theta^*) = m \left(\frac{1}{B_0} \right)^n \exp\left(\frac{3C}{(\theta_r - \theta^*)^K} - \frac{Q}{R\theta^*} \right) \tag{3.8}$$

with m representing an adjustable flow enhancement factor, B_0 and C represent flow rate factors, K represents a flow rate exponent, θ_r represents the triple point temperature of water, Q represents the activation energy for creep, R represents the universal gas constant, θ^* is the pressure adjusted temperature of the ice with

$$\theta^* = \theta + \beta \cdot p \tag{3.9}$$

where β represents the pressure dependence of melting. Here, a value of m =1 is used.

The total motion of the glacier is a combination of internal deformation of the ice and sliding where the interface between the ice and the bed is lubricated by meltwater. Interior velocities are initialized in the model by adding the basal velocity to the temperature-dependent internal deformation. Boundary conditions are set for the momentum balance equation as described in the following sections.

3.2.2 Boundary Conditions

The domain has four distinct boundaries: (1) the upper surface, (2) the bed, (3) the upstream end of the glacier, and (4) the downstream end of the glacier.

3.2.2.1 Upper Surface Boundary Conditions

The upper surface of the glacier is considered stress-free

$$\left[-p\mathbf{I}+\eta\left(\nabla\mathbf{u}+(\nabla\mathbf{u})^{T}\right)\right]\hat{n}=0 \qquad (3.10)$$

in which I is an identity matrix and $\hat{n}$ is the unit vector, pointing outward normal to the boundary. Conservation of mass along the upper surface is set to zero for steady state models while still allowing for vertical movement of ice across the boundary.

3.2.2.2 Basal Boundary Conditions

The bed of the glacier is subject to a no-slip condition in some scenarios and obeys a sliding law in others. In either case basal melting is assumed to be zero, so the vertical component of the velocity vector (w_b) is set to zero at the base. This condition is set because the temperature is only an estimate. In the no-slip boundary case, horizontal velocity at the bed, u_b is set to zero:

$$u_b = 0 \qquad (3.11)$$

In the case of sliding an empirical relationship must be used to compute the magnitude of the sliding velocity. Regions predicted to have basal temperature below the pressure melting point are not allowed to slide. Several sliding relations have been proposed, (for example Bindschadler, 1983; Vieli et al., 2000). Basal water pressure has been shown to greatly affect the sliding velocity of tidewater glaciers (Iken, 1981; Jansson, 1995; Kamb et al., 1994; Meier et al., 1994). Crane Glacier is a tidewater glacier and at the terminus 91% of the ice thickness is below sea level so it is reasonable to expect that basal water pressure would act as a primary control on sliding. In this study the sliding law proposed by Bindschadler (1983) is used

$$u_b = k\tau_b^q p_e^{-1} \tag{3.12}$$

in which τ_b represents the basal shear stress, and k and q are adjustable positive parameters. The effective pressure p_e

$$p_e = p_i - p_w \tag{3.13}$$

is the difference between ice overburden pressure p_i and subglacial water pressure p_w. The effective pressure is not allowed to fall below an arbitrary value of 600 kPa. This prevents downstream velocities from becoming excessively large. Water pressure is

$$p_w = \rho_w \cdot g \cdot (h_w - B) \tag{3.14}$$

in which, ρ_w represents the density of water, B represents the basal surface elevation, and h_w represents the water level elevation. In the model, the water pressure is not allowed to become negative. The water level elevation is computed using a linear function

$$h_w = w_x \cdot x + z_0 \tag{3.15}$$

in which w_x represents water level slope and z_0 represents sea level elevation. Models with basal sliding are initialized with a specified basal velocity that is related to the driving stress.

3.2.2.3 Upstream Boundary Conditions

In experiments using the non-scaled coordinate system, a stress continuity equation is used at the upstream end.

$$\begin{aligned} \frac{\partial \sigma_{xx}}{\partial x} &= 0 \\ \frac{\partial \sigma_{xz}}{\partial x} &= 0 \\ \frac{\partial \sigma_{zz}}{\partial x} &= 0 \end{aligned} \tag{3.16}$$

In experiments using the scaled coordinate system in a limited reach of the glacier, horizontal and vertical components of velocity are prescribed at the upstream boundary. The velocities specified at each node are interpolated from a steady-state model in a non-scaled coordinate system.

3.2.2.4 Downstream Boundary Condition

The downstream end is treated as either abutting more ice or abutting water and air. In the pre-shelf collapse scenario, the pressure condition is

$$p = \rho_i g(S - z) \tag{3.17}$$

A small back-stress (p_{bs}) of 5 kPa is included in the longitudinal stress term of the of stress balance of downstream boundary in models where the ice shelf is still present. This accounts for the effect of non-local stress balance in the floating ice shelf. The value was determined by examination of stress fields computed by Scambos et al. (2000), in a model of the Larsen B ice shelf. For post-collapse scenarios, p_{bs} is zero and,

$$p = \begin{Bmatrix} 0 & air: \quad z > z_0 \\ \rho_{sw} g \cdot (z_0 - z) & water: z \le z_0 \end{Bmatrix} \tag{3.18}$$

where z_0 represents sea-level elevation, and ρ_{sw} represents the density of seawater. The pressure condition at the downstream end of the glacier is written in terms of stress balance

$$\sigma_{xx} = p + p_{bs} \tag{3.19}$$

3.3 Scaled Coordinate System

Adopting a scaled coordinate system simplifies tracking the ice surface in time-transient simulations. The system of equations is scaled in the vertical direction using a coordinate transformation (Pattyn, 2003)

$$z \to \zeta = \frac{z - B}{S - B} = \frac{z - B}{H} \tag{3.20}$$

This results in a coordinate system in which $\zeta = 1$ at the upper surface and $\zeta = 0$ at the base of the glacier. This transformation maps (x,z) to (x', ζ), so that the function derivatives transform to

$$\frac{\partial f}{\partial x} = \frac{\partial f}{\partial x'}\frac{\partial x'}{\partial x} + \frac{\partial f}{\partial \zeta}\frac{\partial \zeta}{\partial x} \tag{3.21}$$

and,

$$\frac{\partial f}{\partial z} = \frac{\partial f}{\partial \zeta}\frac{\partial \zeta}{\partial z} \tag{3.22}$$

These equations can be simplified

$$\frac{\partial f}{\partial x} = \frac{\partial f}{\partial x'} + a_x \frac{\partial f}{\partial \zeta} \tag{3.23}$$

where

$$a_x = -\frac{1}{H}\left(\zeta \frac{\partial S}{\partial x} + \frac{\partial B}{\partial x}(1-\xi)\right) \tag{3.24}$$

and

$$\frac{\partial f}{\partial z} = \frac{1}{H}\frac{\partial f}{\partial \zeta} \tag{3.25}$$

3.3.1 Transformation of field equations

The Navier-Stokes equations are transformed to

$$\frac{\partial}{\partial x'}E_{xx} + a_x \frac{\partial}{\partial \xi}E_{xx} + \frac{1}{H}\frac{\partial}{\partial \xi}E_{xz} = 0 \tag{3.26}$$

and

$$\frac{\partial}{\partial x'}E_{xz} + a_x \frac{\partial}{\partial \xi}E_{xz} + \frac{1}{H}\frac{\partial}{\partial \xi}E_{zz} = -\rho_i g \tag{3.27}$$

where

$$E_{xx} = 2\eta\left(\frac{\partial u}{\partial x'} + a_x \frac{\partial u}{\partial \xi}\right) - p \tag{3.28}$$

and

$$E_{xz} = \eta\left(\frac{\partial w}{\partial x'} + a_x \frac{\partial w}{\partial \xi} + \frac{1}{H}\frac{\partial u}{\partial \xi}\right) \qquad (3.29)$$

and

$$E_{zz} = 2\eta\left(\frac{1}{H}\frac{\partial w}{\partial \xi}\right) - p \qquad (3.30)$$

3.3.2 Transformation of boundary conditions

The stress condition at the downstream end of the glacier (Equation 3.19) is

$$E_{xx} = p + p_{bs} \qquad (3.31)$$

3.4 Model Setup: Boundary Conditions and Constants

3.4.1 Internal Temperature

The rate factor in the flow law requires an estimate of ice temperature yet, there are no direct observations for temperature in the interior of Crane Glacier. A simple estimate of ice temperature is made here. Ignoring horizontal advection and strain heating, a temperature profile can be computed using two thermal boundary conditions (Hooke, 2005):

$$\theta(x,z) = \theta_s - \frac{\sqrt{\pi}}{2}\frac{G}{\zeta_0}[erf(\xi_0 H) - erf(\xi_0 z)] \qquad (3.32)$$

where θ represents temperature, G represents the basal temperature gradient,

$$\zeta_0 = \sqrt{\frac{b_n}{2\kappa H}} \qquad (3.33)$$

in which, b_n represents the upper surface mass balance, κ represents thermal diffusivity of ice, surface temperature θ_S is specified by

$$\theta_S = \theta_S^{'} + x \cdot \lambda \tag{3.34}$$

and the error function

$$erf(x) = \frac{2}{\sqrt{\pi}} \int_0^x e^{-t^2} dt \tag{3.35}$$

has been tabulated.

Equation 3.32 is inappropriate where the basal temperature reaches the local (pressure-dependent) melt temperature. At locations where Equation 3.32 predicts an ice temperature above freezing and basal melting is implied. The basal temperature gradient is adjusted in Equation 3.32 so that ice at the base is at the pressure-melting point. Constants used in this calculation are summarized in Table 3.3.

Table 3.3 Constants used in temperature profile calculation.

symbol	value
θ'_s	-5 C
λ	-0.0044 K m^{-1}
G	0.026 K m^{-1}
b_n	0.82 m a^{-1}

Values for surface temperature at sea level, surface mass balance and lapse rate are based on observation and model fields reported in the literature (Section 2.6). The heat flux used here, 60 W m^{-2} (.026 K m^{-1}, ice equivalent) falls within the range of values (50 to 65 W m^{-2}) published in a magnetic heat flux anomaly study for the Antarctic continent (Maule et al., 2005). The temperature solution (Figure 3.4) indicates that basal ice goes below the local melting point significantly upstream (~30 km) and the furthest upstream reach is significantly colder at the base (6-7 ºC).

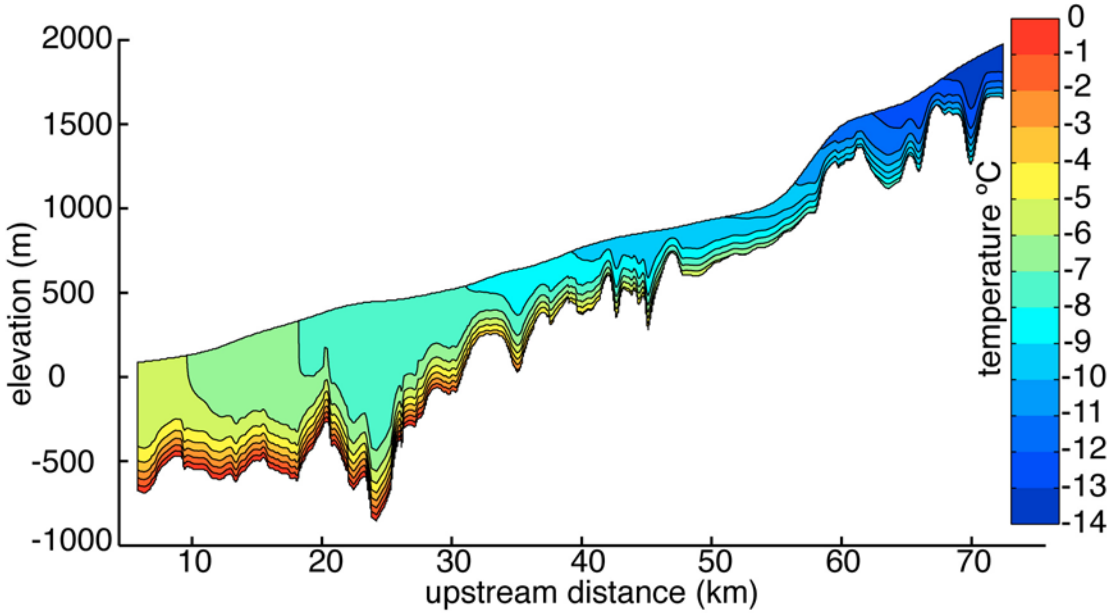

Figure 3.4 Temperature profile predicted by equation solving for diffusion and vertical advection of ice.

3.4.2 Viscosity

Initial attempts to solve the conservation equations in the scaled coordinate system using the Glen flow law failed to converge. The solution to this impasse is to specify a fixed viscosity field rather than computing the viscosity as a part of the solution. The viscosity is determined by solving the momentum balance equations without basal sliding using a non-scaled system. The resulting viscosity is then used in model experiments (Figure 3.5).

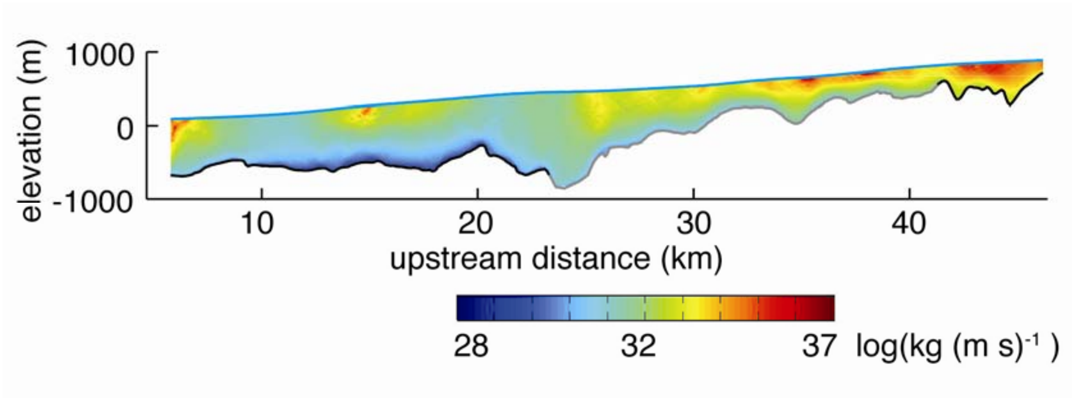

Figure 3.5 Viscosity from model using temperature profile predicted by Equation 3.32.

3.4.3 Validation of Momentum Balance

The numerical solution to the momentum balance may be validated by comparing the analytical solution for local balance (Equation 2.3) with a deformation-only model surface velocity. The comparison is not exact because the model includes both vertical shear (as in the analytical solution) and longitudinal stress. Nevertheless, there should be a general agreement between the two.

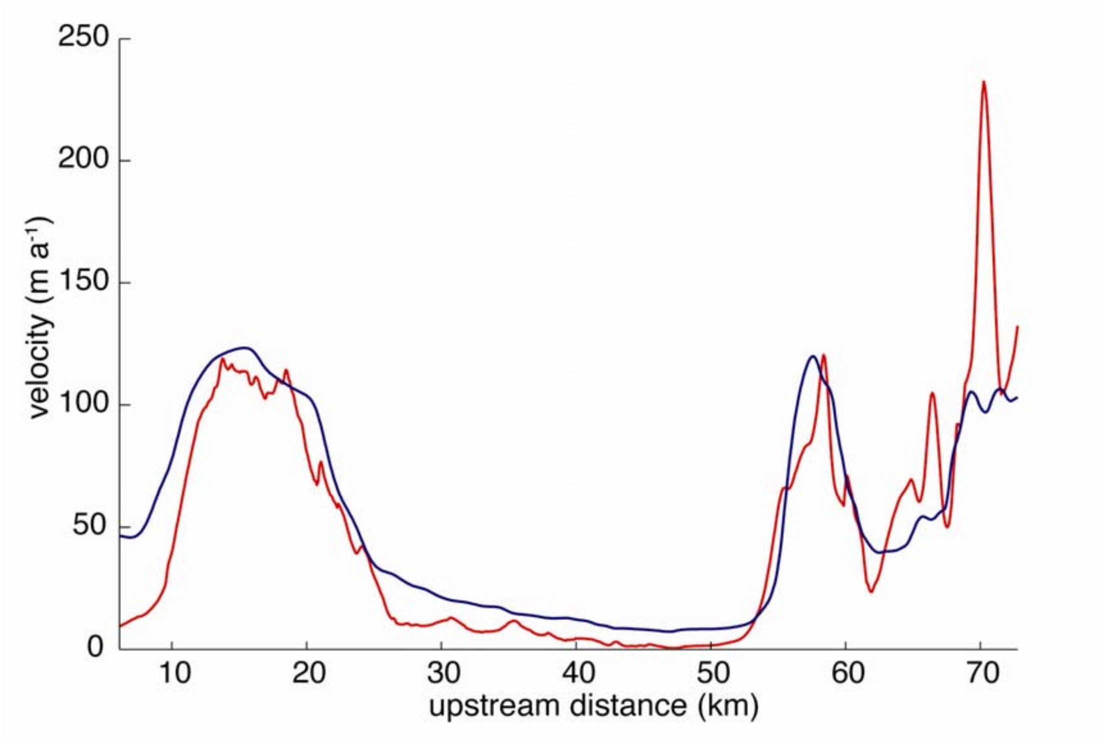

Figure 3.6 Predicted surface velocities from numerical model (blue) and analytical approximation (red) match well indicating the deformation model works as expected.

The Glen flow law is used with a uniform temperature of -5 ºC. This relatively warm temperature is appropriate for deep ice, where most of the deformation takes place. Surface velocities from the analytical solution have been smoothed over several ice-thicknesses to facilitate comparison with the numerical model for which the bed elevation has been smoothed. While details vary, the magnitudes of the two solutions agree well (Figure 3.6). Because the numerical solution includes longitudinal stress while the analytical solution does not, the numerical solution is relatively smooth, an expected result. Overall, the numerical solution to the momentum balance equations performs as expected (Figure 3.7).

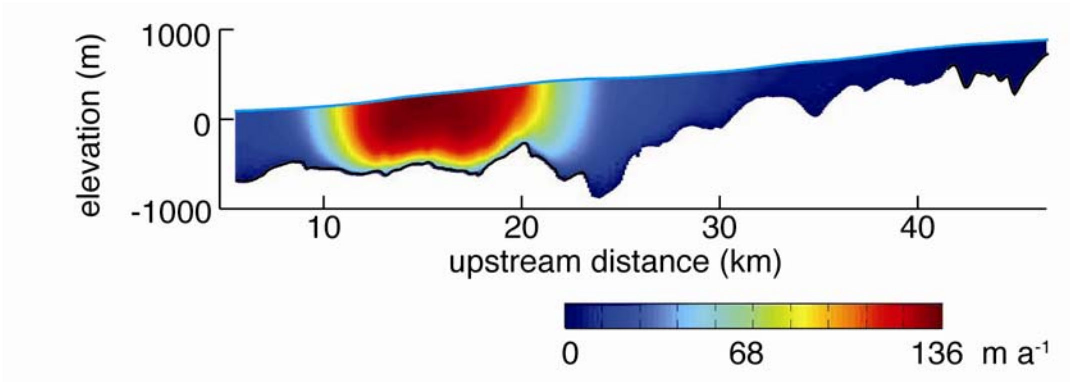

Figure 3.7 Computed deformation velocity for Crane Glacier profile using the Glen flow law and the estimated temperature profile.

3.4.4 Sliding

Before the model can be used to investigate glacier change, it is important to first demonstrate that Crane Glacier is indeed sliding along its base. The deformation-only model is used to evaluate glacier sliding (Figure 3.8). Where deformation-only surface speed agrees well with observed pre-collapse speed, the glacier is not sliding. Where the quantities differ by more than measurement error, sliding is likely. The large (~5 times at the downstream end) discrepancy between the observed surface velocity and the surface velocity for deformation only clearly demonstrates that Crane Glacier is sliding along its base.

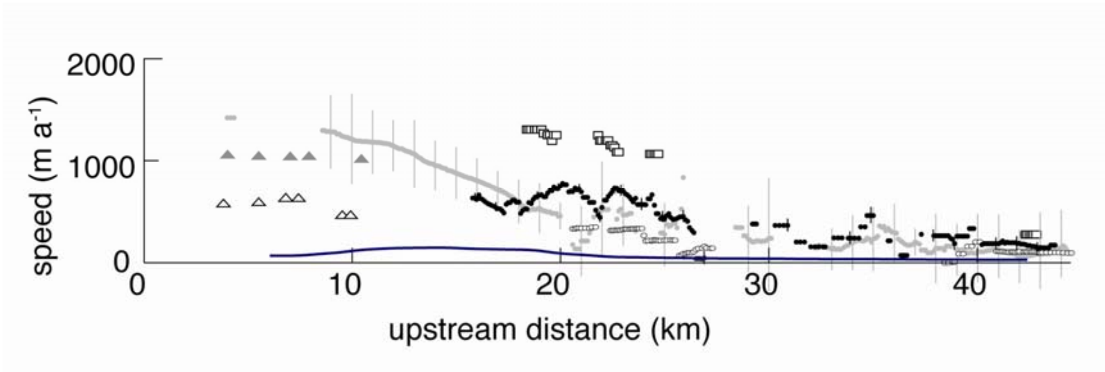

Figure 3.8 Surface velocities observations are shown time periods: from 27 January 2000 to 06 December 2001 (hollow triangles), from 06 December 2001 to 18 December 2002 (filled triangles), from 18 December 2002 to 20 February 2003 (filled grey circles), from 18 December 2002 to 13 January 2004 (filled black circles), from 13 January 2004 to 27 September 2004 (hollow circles) and, from 24 November 2005 to 25 November 2006 (hollow squares). Surface velocities from a deformation-only model are in blue.

The deformation speed computed in Section 3.4.3 is used for the sliding analysis. The uniform temperature of -5ºC used in that calculation is warmer than the estimated internal temperature. Warmer temperatures decrease $A(\theta^*)$ in Equation 3.8 and therefore decrease viscosity η in Equation 3.6. The overall effect of using a relatively warm internal temperature is to over-predict surface velocity.

3.4.5 Setup for Determining Sliding Parameters

A sliding parameterization based on the water pressure at the bed of the glacier is used to approximate the basal sliding speed (Equation 3.12). The rate factor k and internal water level slope w_x vary from glacier to glacier. Here, these parameters are tuned to reproduce velocities observed at the surface of Crane Glacier prior to ice shelf collapse.

A parameter space search is used in which both *k* and the height of water at the upstream end of the domain Δwl are adjusted through a range of possible values, where

$$\Delta wl = w_x \cdot L \tag{3.36}$$

in which *L* represents the length of the domain. The model is run a number of times, adjusting the parameter values so that each combination of parameters is examined.

There is not a complete set of observed surface velocities $u_s(obs)$ prior to collapse. Pre- and post-collapse data must be combined in order to establish a velocity profile useful for parameter tuning. Care is taken to omit the data used to estimate missing bed elevations (Section 2.1) from the sliding parameter analysis. Pre-collapse velocity information is available at the most downstream end of the glacier. Velocity in the far upstream reach did not change following ice shelf collapse; therefore data in the upstream reach may be used to represent its pre-collapse condition. The surface velocities observed from February 2003 to January 2004 may be used in the region where the bed geometry was not directly measured on the NASA/KU/CECS flightline (Figure 3.9).

Four observed velocity data sets were used in the sliding parameter estimation. Sets were made with and without the February 03 to February 04 velocity data in the region where ice thickness was estimated using surface velocity. Because the velocities from the feature tracking are interpolated to the flightline it is also important to evaluate how the search radius used in that process may affect the parameter estimation. To this end, target data sets are created using both 500 m and 1000 m search radii (for comparison, glacier width is approximately 8 km in the downstream reach).

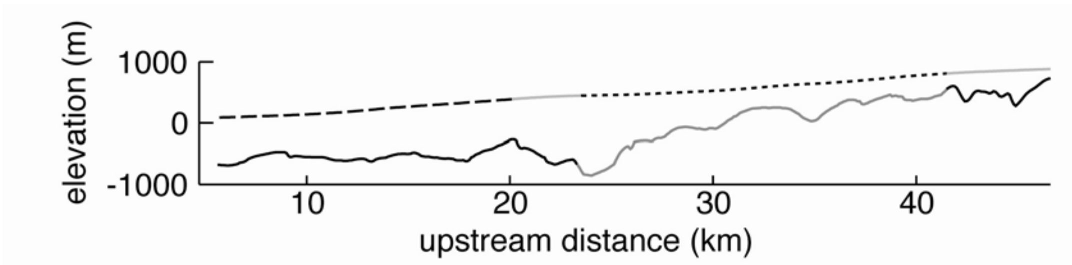

Figure 3.9 A combination of data from different epochs is used as a basis for comparison to the model output for surface velocity. Time periods used are: from 27 January 2000 to 06 December 2001 (long dashed black line), from 18 December 02 to 20 February 2003 (light grey line) and, from 18 December 2002 to 13 January 2004 (short dashed black line).

A least-squares technique is used to compare model surface velocities $u_s(model)$ to those observed for each model run (Björck, 1996). The model surface velocities are interpolated onto flightline spacing using a linear interpolation. The sum of squares *SS* is

$$SS = \sum W \cdot r^2 \tag{3.37}$$

where

$$W = \frac{1}{{\sigma_v}^2} \tag{3.38}$$

in which σ_v represents the error on the observed surface velocities and

$$r = u_s(model) - u_s(obs)\,. \tag{3.39}$$

in which u_s represents the upper surface velocity. The set of parameters that minimize *SS* are selected and set as constant parameters in experiments with sliding. In effect, the ratio of k/p_e is being tuned.

The parameters were adjusted in model runs through a range of reasonable values. Here, k was varied between 14.3×10^{-15} and 19.0×10^{-15} m s^{-1} Pa^{-2} (4500 and 6000 m a^{-1} bar^{-2}) using 0.8×10^{-15} m s^{-1} Pa^{-2} (250 m a^{-1} bar^{-2}) increments and Δwl was varied between 0 and 100 m using 25 m increments. *SS* was calculated for each pair of tuning parameters (Figure 3.10) for each of the four scenarios, with or without fill data and using 500 m or 1000 m search radii (Figure 3.11).

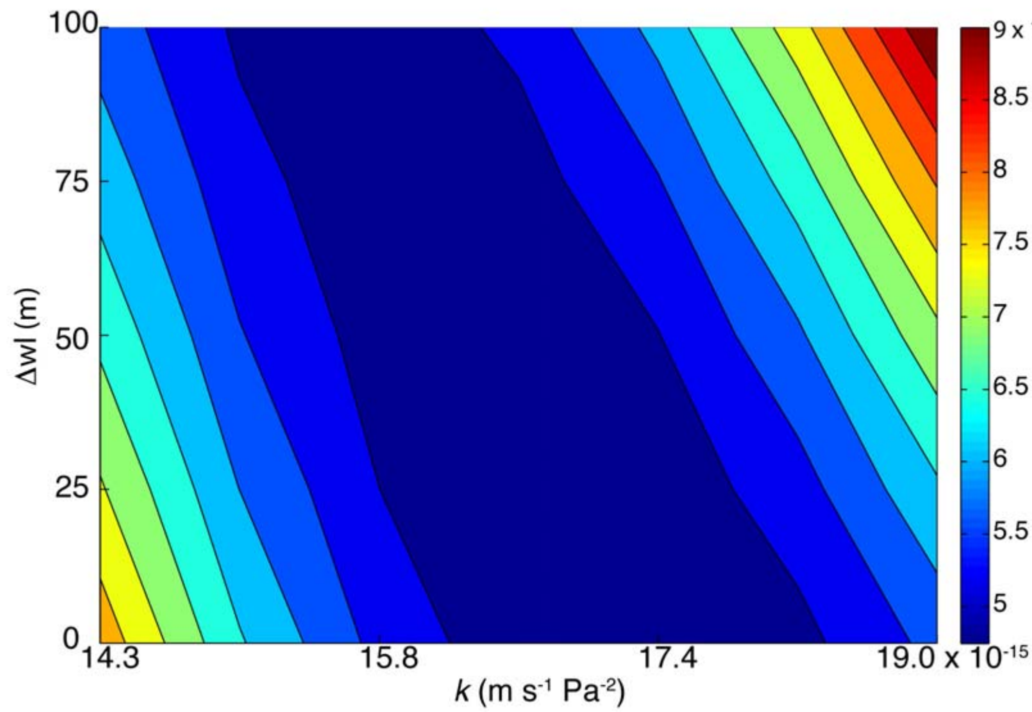

Figure 3.10 Sum of squares (*SS*) calculation over parameter space varying *Δwl* and *k* for the 500m search radius with no fill comparison.

Each of the four scenarios, with or without fill data and using 500 m or 1000 m search radii, indicated the upstream water elevation of 0m. The optimal value of *k* varied between 16.6×10^{-15} to 17.4×10^{-15} m s^{-1} Pa^{-2} (5250 to 5500 m a^{-1} bar^{-2}) in cases with a 1000 m search radius and a 500 m search radius respectively. Since overall errors were smaller in cases using a 500m search radius, the sliding parameter of 17.4×10^{-15} m s^{-1} Pa^{-2} (5500 m a^{-1} bar^{-2}) was chosen. The driving stress is not balanced locally by the basal drag. This is about an order of magnitude greater than values published, 4 to 128 m a^{-1} bar^{-2} (0.01×10^{-15} and 0.4×10^{-15} m s^{-1} Pa^{-2}) in (Bindschadler, 1983) and 400 to 550 m a^{-1} bar^{-2}(1.3×10^{-15} and 1.7×10^{-15} m s^{-1} Pa^{-2}) in (Vieli et al., 2000). However, the sliding law coefficient used reproduced observed surface velocities well when an estimation of basal shear stress based on lithostatic pressure and basal slope is used in Equation 3.12.

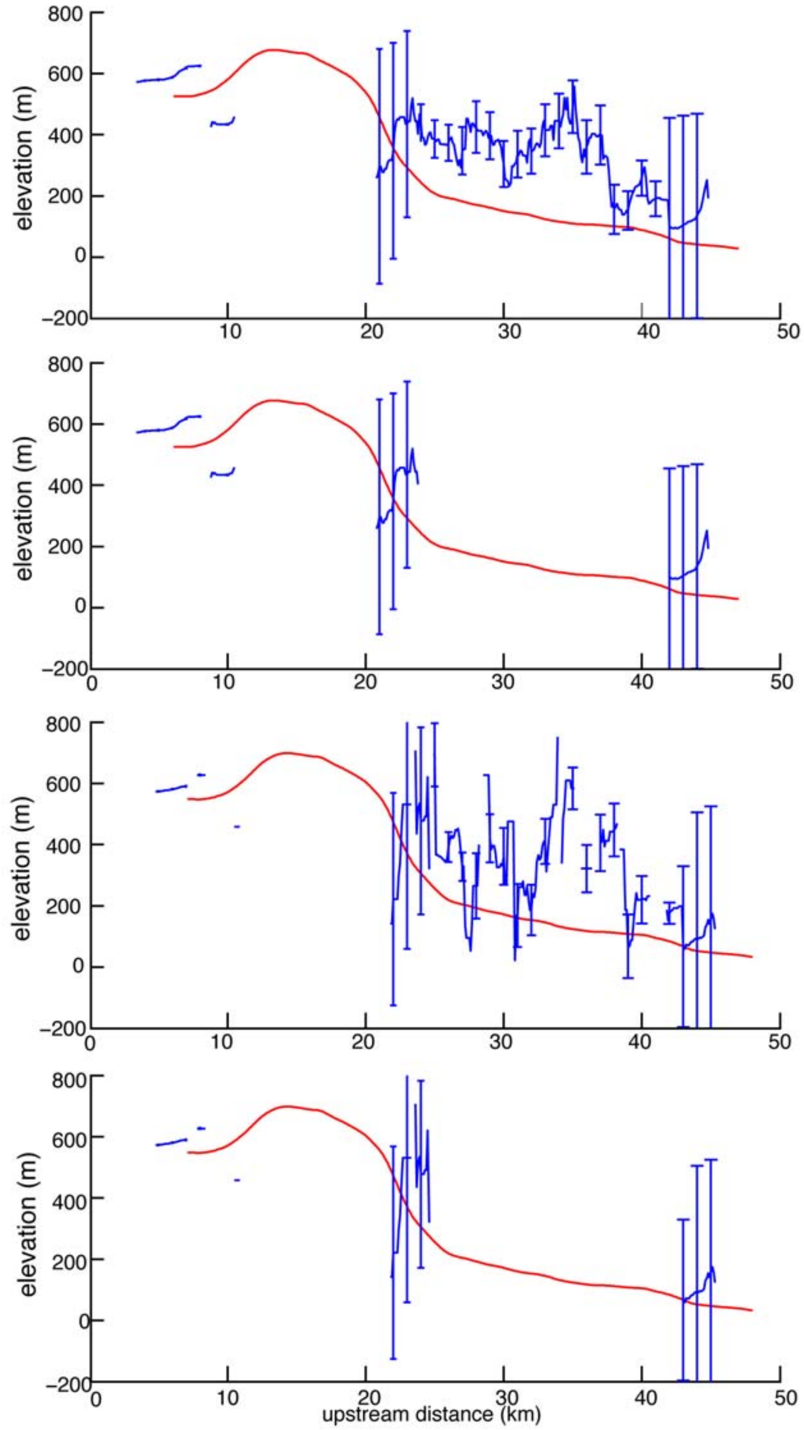

Figure 3.11 Surface velocity of tuned model (red) compared to observations (blue). Error bars on blue represent one standard deviation. Upper graph shows 500 m search radius with fill comparison, upper-middle graph shows 500 m search radius with no fill comparison, lower-middle graph shows 1000 m search radius with fill comparison and lower graph shows 1000 m search radius with no fill comparison.

4 Model Application

4.1 Ratio of the Width to Thickness and Glacier Momentum Balance

One explanation of the differences among glacier response to ice shelf collapse in the Larsen B embayment is the effect of glacier geometry on the partitioning of resistive stresses in the glaciers. Relatively wide glacier may be able to respond rapidly to the stress perturbation at their downstream ends because side drag is less important across more of the glacier width than is the case on relatively narrow glaciers. This geometric effect is demonstrated by solving the full momentum balance in a simple 3-dimensional trough. We are interested primarily in the relation between lateral drag σ_{xy} and longitudinal stress σ_{xx}.

The model domain is in effect a trough of uniform width, thickness, and slope. Boundary conditions are applied to represent pressure of ice at the upstream and downstream ends of the glacier, no-slip conditions along the sidewalls and an open boundary along the top. The model uses a Glen flow law rheology at a uniform temperature of -5 °C throughout the domain. The steady state momentum equation is solved for a range of width to thickness ratios (W:H) and slopes (Figure 4.1).

Lateral drag σ_{xy} is largest at the valley walls and goes to zero at the centerline of the trough. The shape of $\sigma_{xy}(y)$ depends on the W:H. At a given location between the margin and the centerline the ratio between lateral shear and longitudinal stress (or between shear strain rate $\dot{\varepsilon}_{xy}$ and longitudinal stretching rate $\dot{\varepsilon}_{xx}$) must accordingly vary with W:H (Figure 4.2).

When W:H is relatively large, $\dot{\varepsilon}_{xx} : \dot{\varepsilon}_{xy}$ is relatively large at off-center and off-margin locations. Larger slope also yields larger $\dot{\varepsilon}_{xx} : \dot{\varepsilon}_{xy}$, and the effect is more pronounced for larger W:H. Thus, we may expect stress perturbations at the downstream end of the glacier transmitted via longitudinal stresses to propagate farther upstream on large W:H glaciers than on small W:H glaciers.

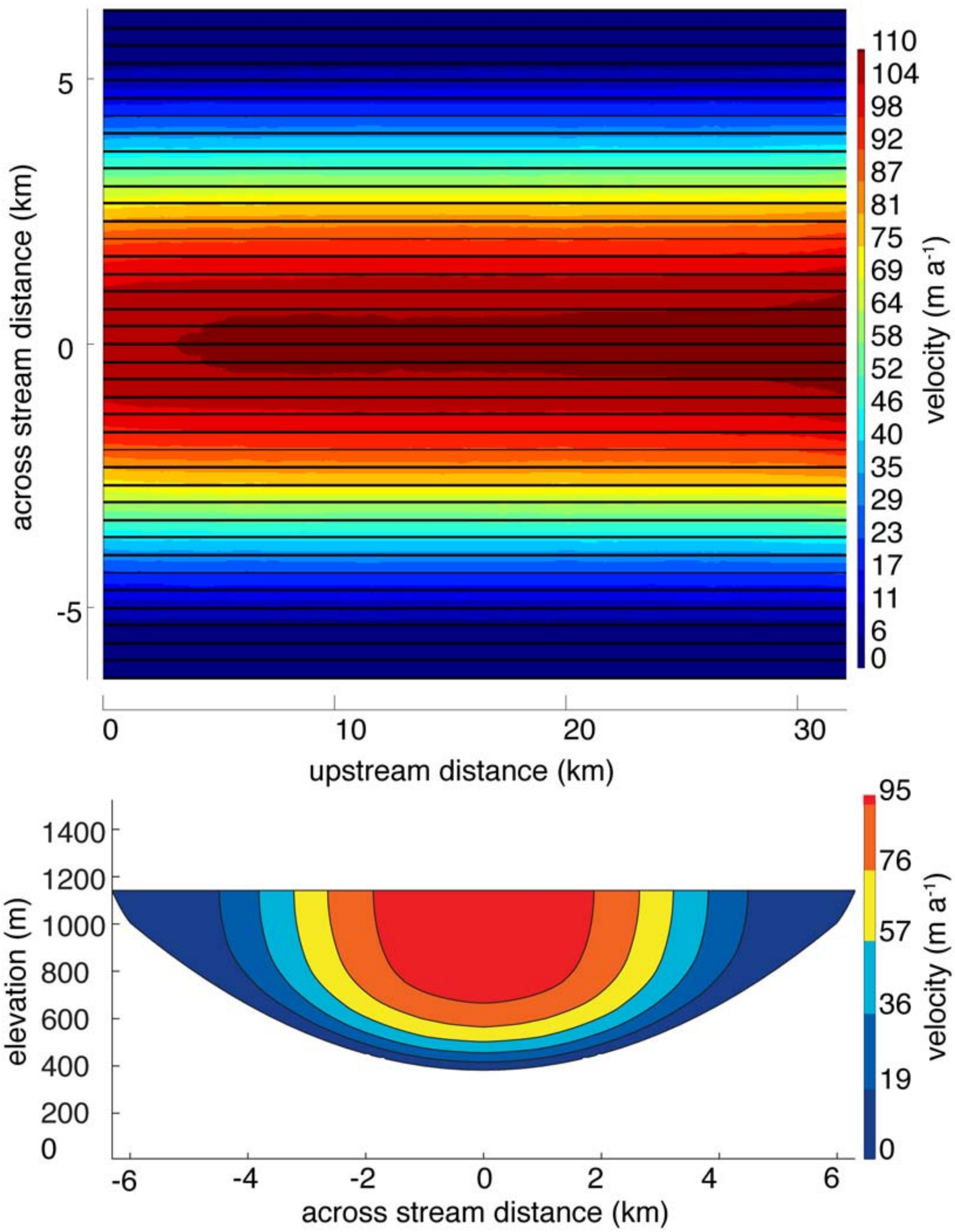

Figure 4.1 Plan view of downstream component of surface velocity (upper) is uniform with upstream distance. Downstream component of velocity for a cross-section (lower) shows faster flow away from boundaries.

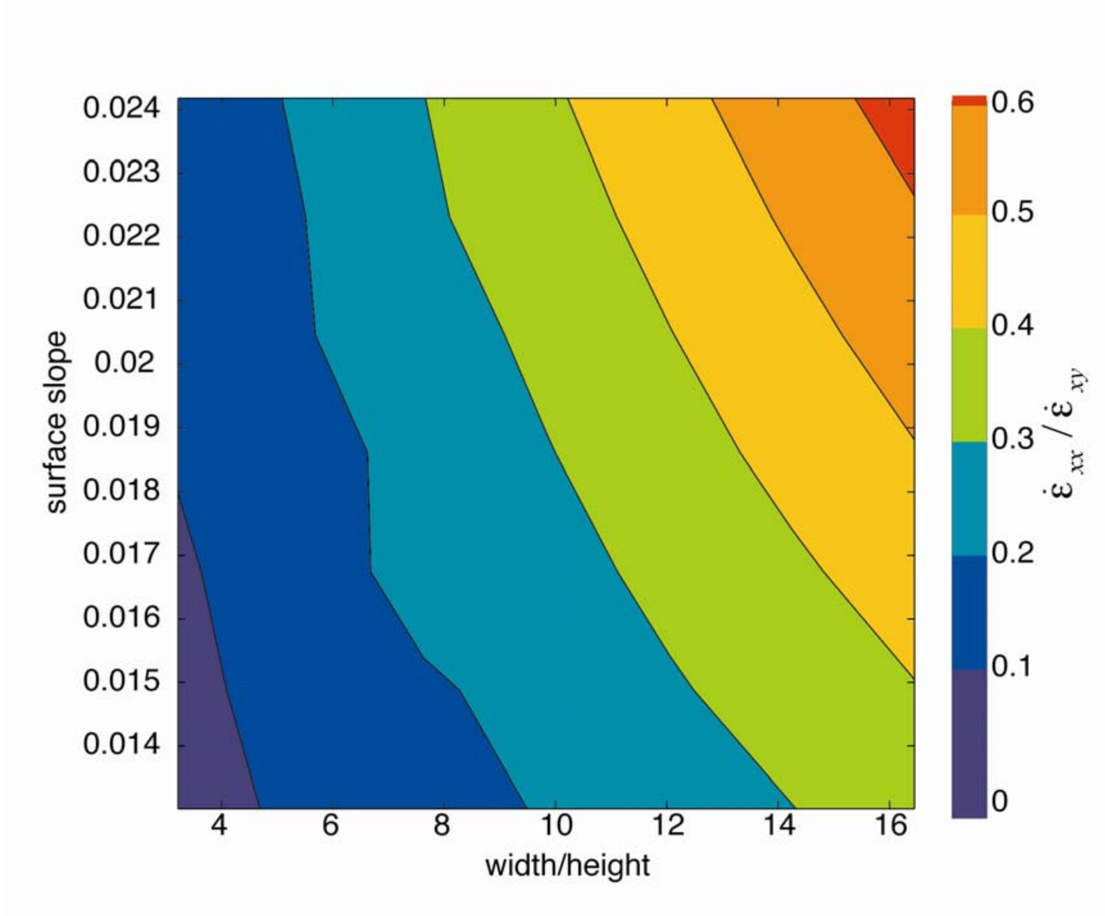

Figure 4.2 The ratio of longitudinal and lateral strain rates for a parameter space of surface slopes and ratios of glacier width to thickness. The model described in Section 4 was sampled at ¼ W. Crane Glacier has a W:H of 10 at its downstream reach.

4.2 Instantaneous Response of Crane Glacier to Ice Shelf Collapse

Instantaneous ice shelf disintegration is simulated in the model by replacing the downstream stress condition representing ice with the stress condition prescribed by Equation 3.18 representing the pressure of air and water. The output model surface velocities are then compared in the pre- and post-collapse conditions. Experiments are conducted for both deformation only and deformation with basal sliding conditions.

4.2.1 Glacier Flow

Velocity and the partitioning of resistive stresses vary among models simulating deformation only or deformation with sliding and with or without ice shelf removal. The model simulating deformation-only has a small surface velocity in the upstream reach (Figure 4.3). As the ice moves closer to a deepening located about 25 km upstream, the surface velocity increases as the thickness increases. The ice begins to stretch and basal shear is reduced as surface slope shallows over the overdeepening. Surface slope and basal shear again increase as ice passes over the bedrock high at 20 km upstream of the glacier terminus. At about 13 km upstream, the driving stress decreases due to lowering surface slope, where the surface speed is reduced longitudinal stress changes from extension to compression (Figure 4.10). In the real glacier, ice here is close to floatation and about to enter the ice shelf.

Following ice shelf removal, in the deformation-only model the resistive stresses and surface velocity largely follow the same spatial distribution as the case with ice shelf presence (Figure 4.4). The exception is in the downstream most end where basal shear, longitudinal stretching, and surface velocity increase. The response of glacier is limited to the region with 10 km of the downstream end of the model domain, a length of about 7 ice thicknesses (Figure 4.8).

In the simulation with basal sliding, surface velocity changes with distance downstream in a similar pattern to the deformation only simulation, but with a change in magnitude (Figure 4.5). Basal shearing closely matches the driving stress throughout the upstream region. As ice moves downstream across the overdeepening basal shear stress becomes larger than the driving stress in response to the onset of sliding. As ice approaches the bedrock high located 20 km upstream the driving stress increases and the ice stretches in order to overcome the obstacle. Once ice has moves over this bump, longitudinal stretching is reduced and surface velocity increases as basal shear drops below the driving stress. At about 13 km upstream of the terminus, the driving stress decreases due to flattening surface slope, the ice compresses and basal shear exceeds driving stress.

Following ice shelf removal, surface velocity increases continuously with distance downstream in the simulation with sliding (Figure 4.6). The response is most pronounced near the front of the glacier. Overall patterns in σ_{xx} and σ_{xz} are similar to the pre-shelf removal results.

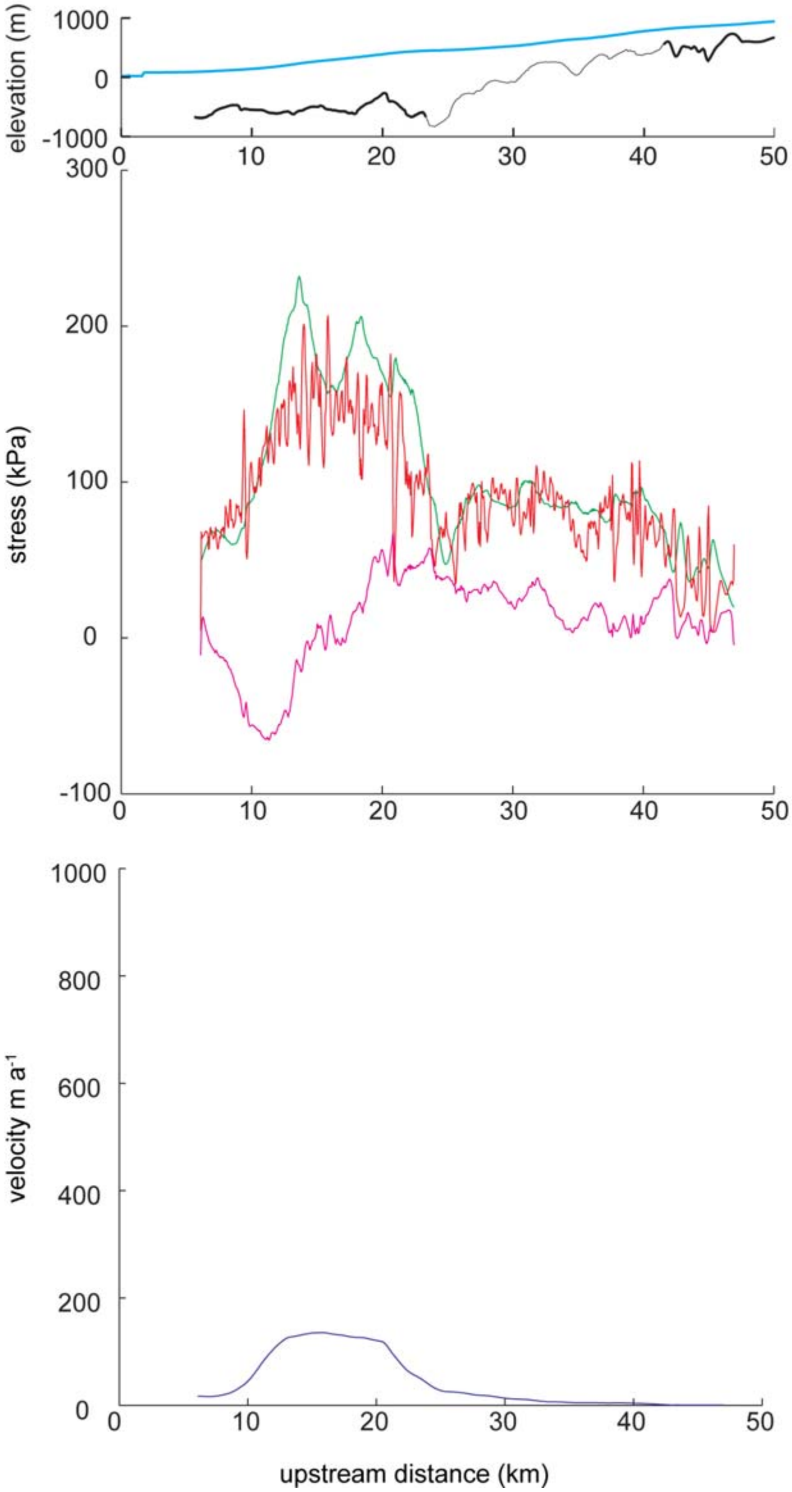

Figure 4.3 Flowline geometry (upper), driving stress (green), basal shear (red) and depth averaged longitudinal stretching (pink; middle), and horizontal component of velocity at surface (lower) are shown for the deformation only model before ice shelf removal.

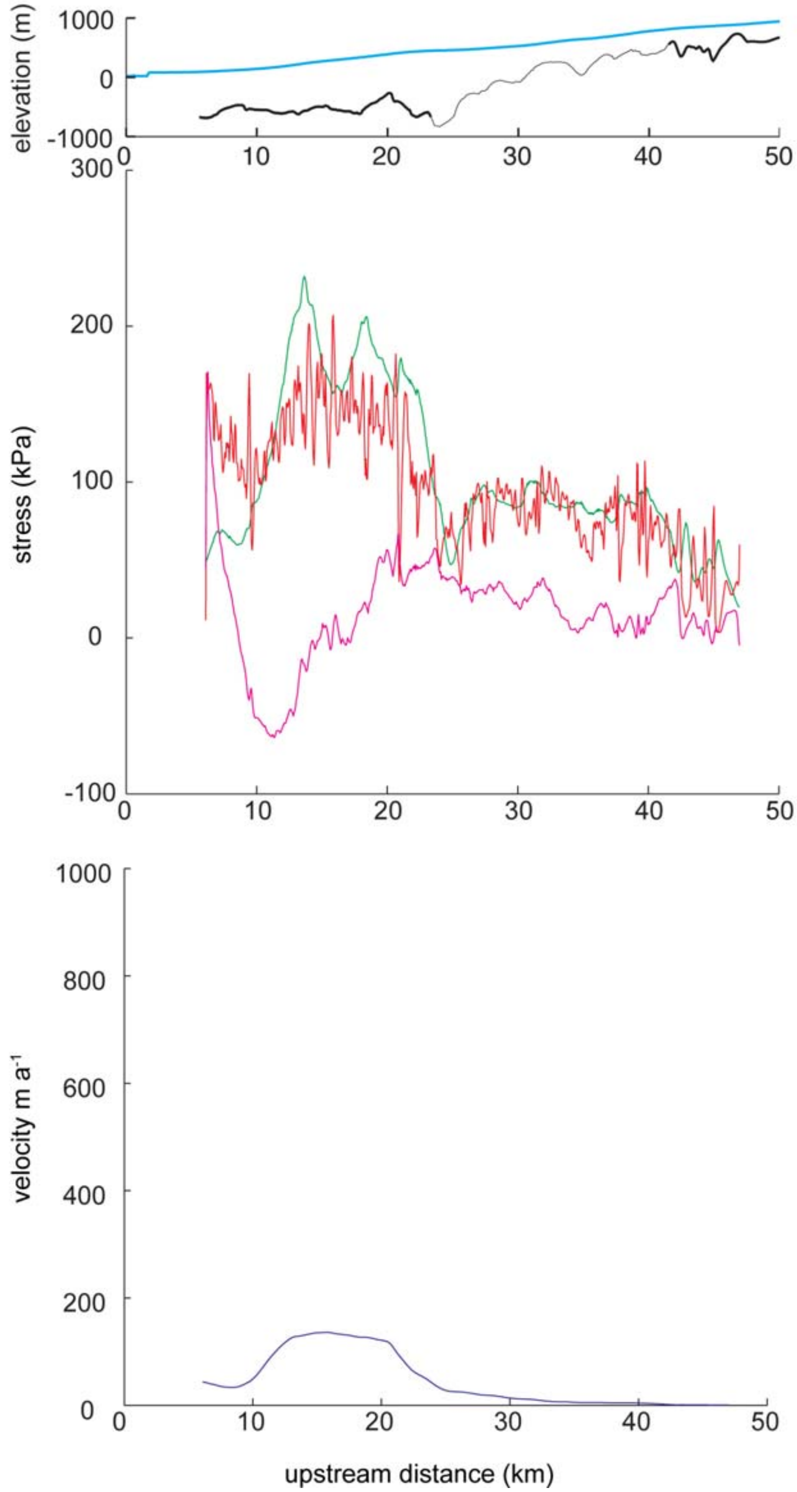

Figure 4.4 Flowline geometry (upper), driving stress (green), basal shear (red) and depth averaged longitudinal stretching (pink; middle), and horizontal component of velocity at surface (lower) are shown for the deformation only model after ice shelf removal.

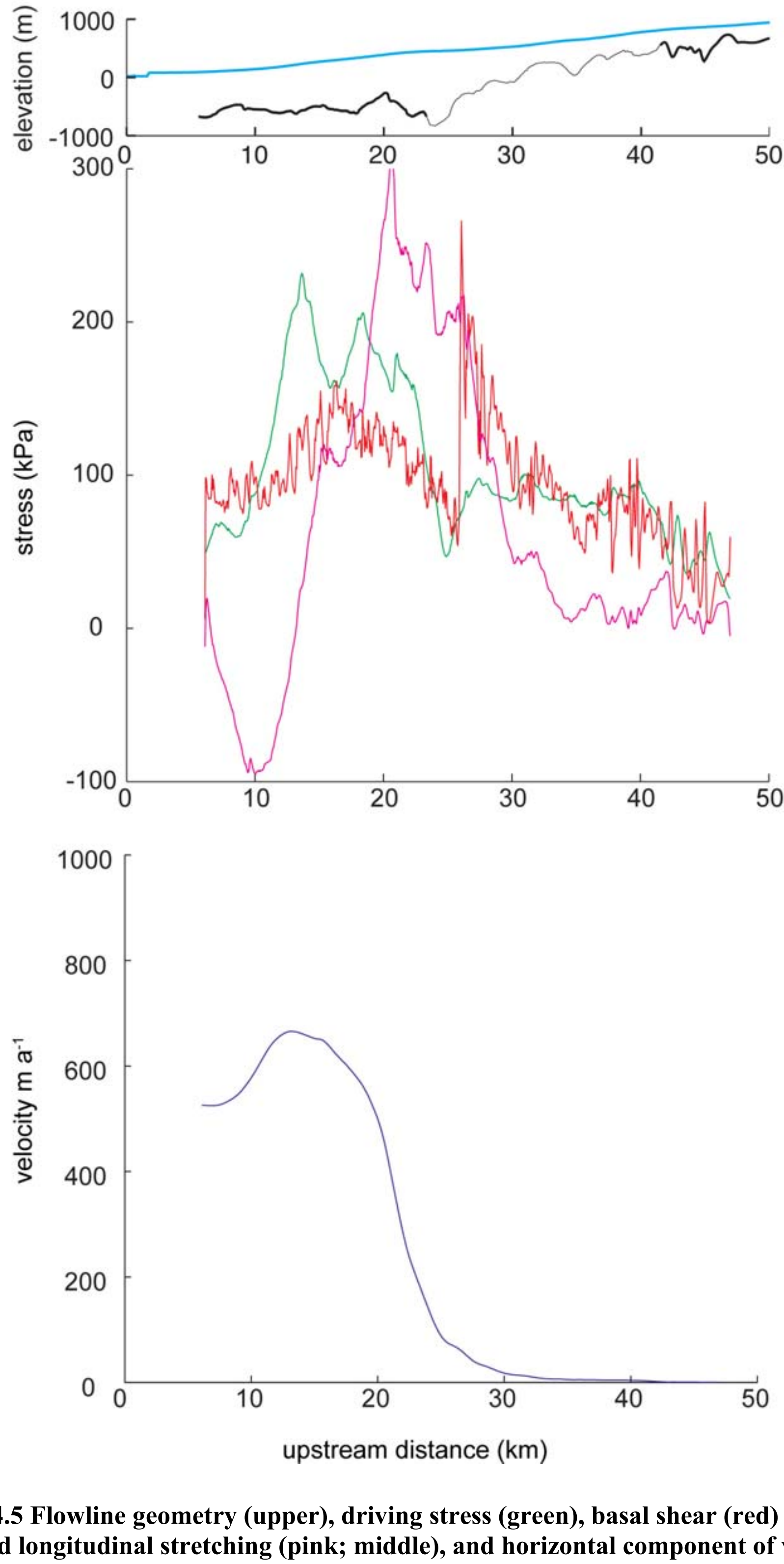

Figure 4.5 Flowline geometry (upper), driving stress (green), basal shear (red) and depth averaged longitudinal stretching (pink; middle), and horizontal component of velocity at surface (lower) are shown for the deformation and sliding model before ice shelf removal.

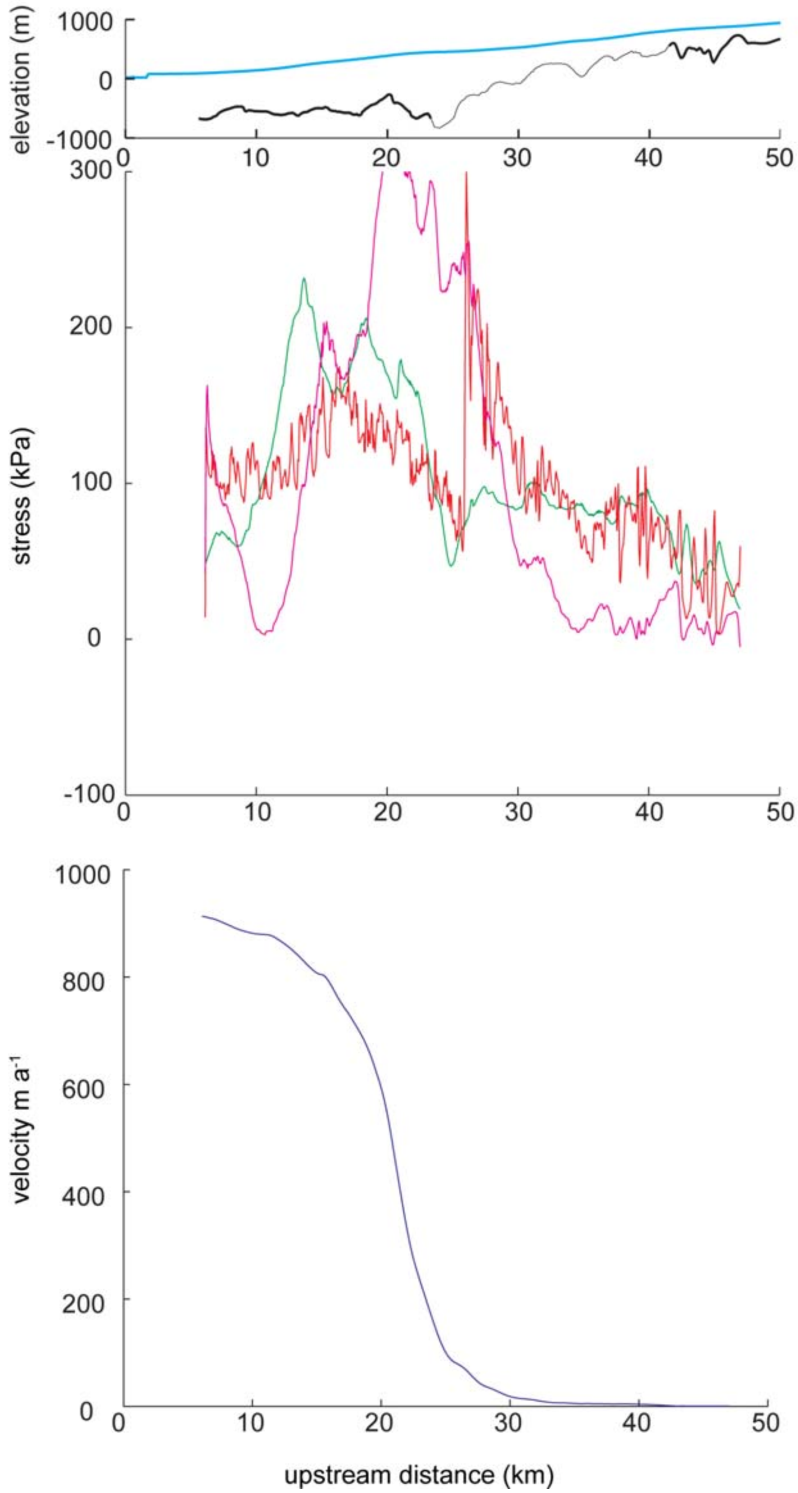

Figure 4.6 Flowline geometry (upper), driving stress (green), basal shear (red) and depth averaged longitudinal stretching (pink; middle), and horizontal component of velocity at surface (lower) are shown for the deformation and sliding model after ice shelf removal.

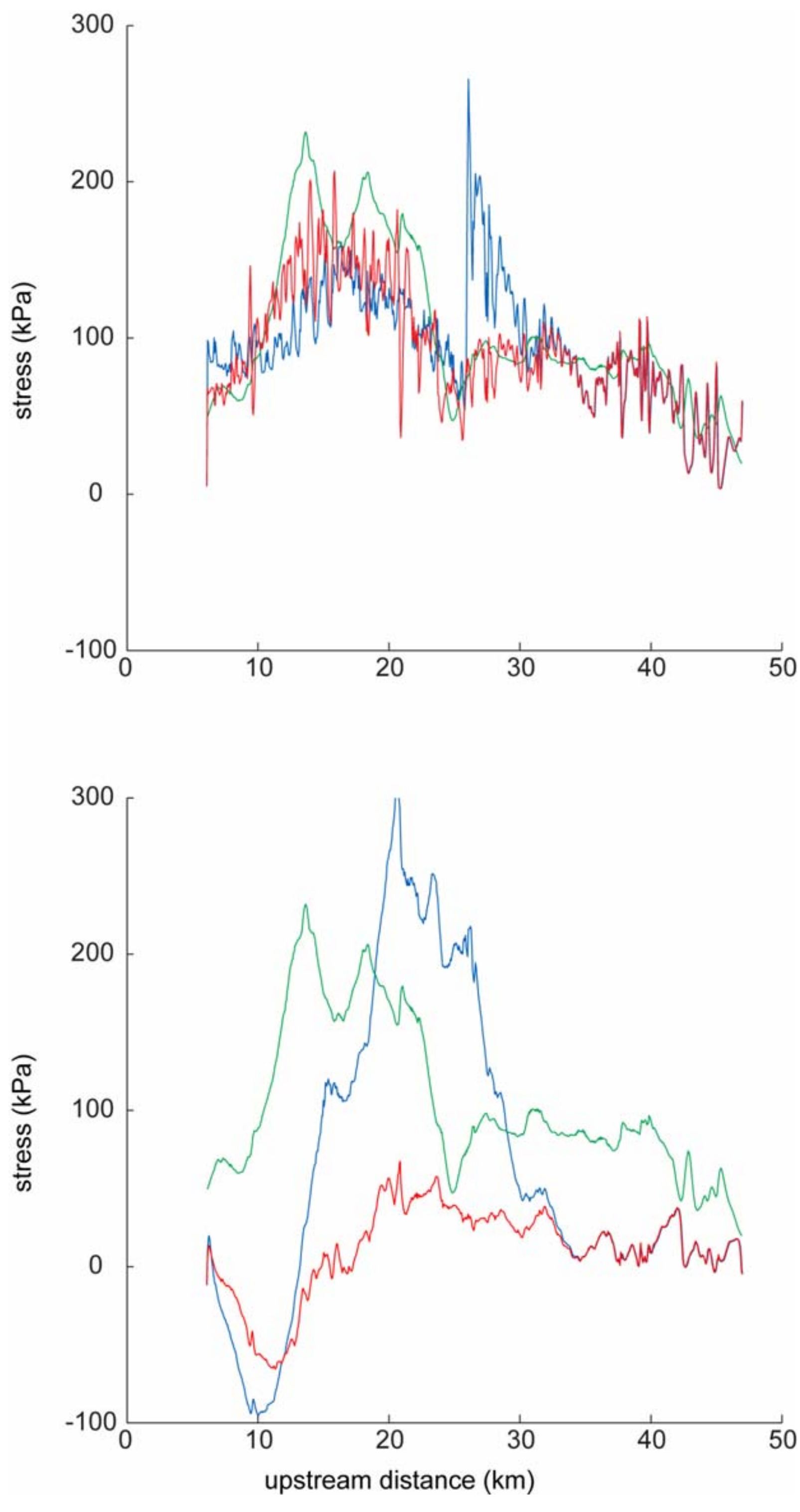

Figure 4.7 Driving stress (green) is compared to the basal shear stress before ice shelf removal, in deformation only model (red) and deformation and sliding model (blue; upper). Driving stress (green) is compared to the longitudinal stress before ice shelf removal, in deformation only model (red) and deformation and sliding model (blue; lower).

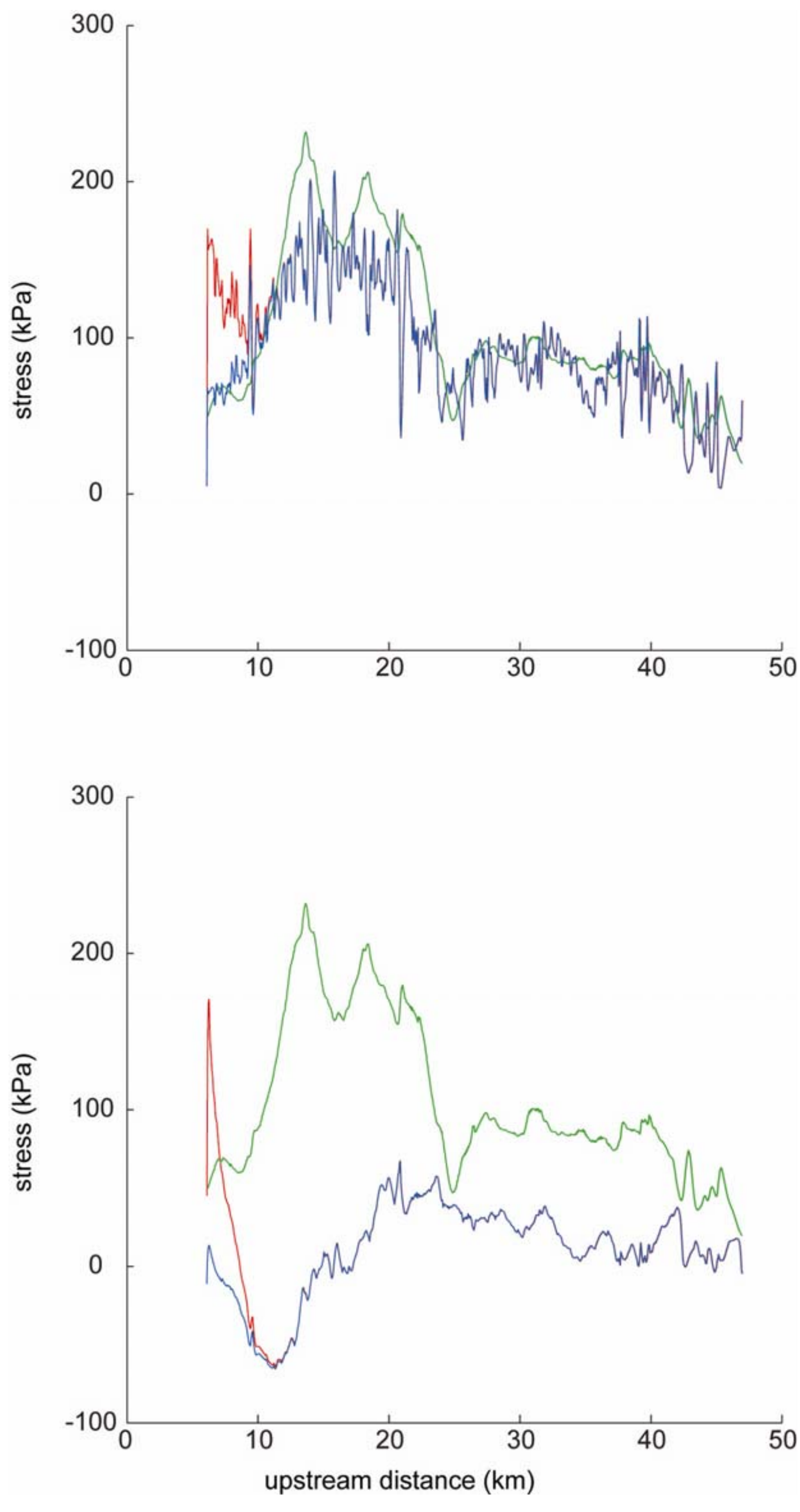

Figure 4.8 Driving stress (green) is compared to the basal shear stress in deformation only model before (blue) and after ice shelf removal (red; upper). Driving stress (green) is compared to the longitudinal stress deformation only model before (blue) and after ice shelf removal (red; lower).

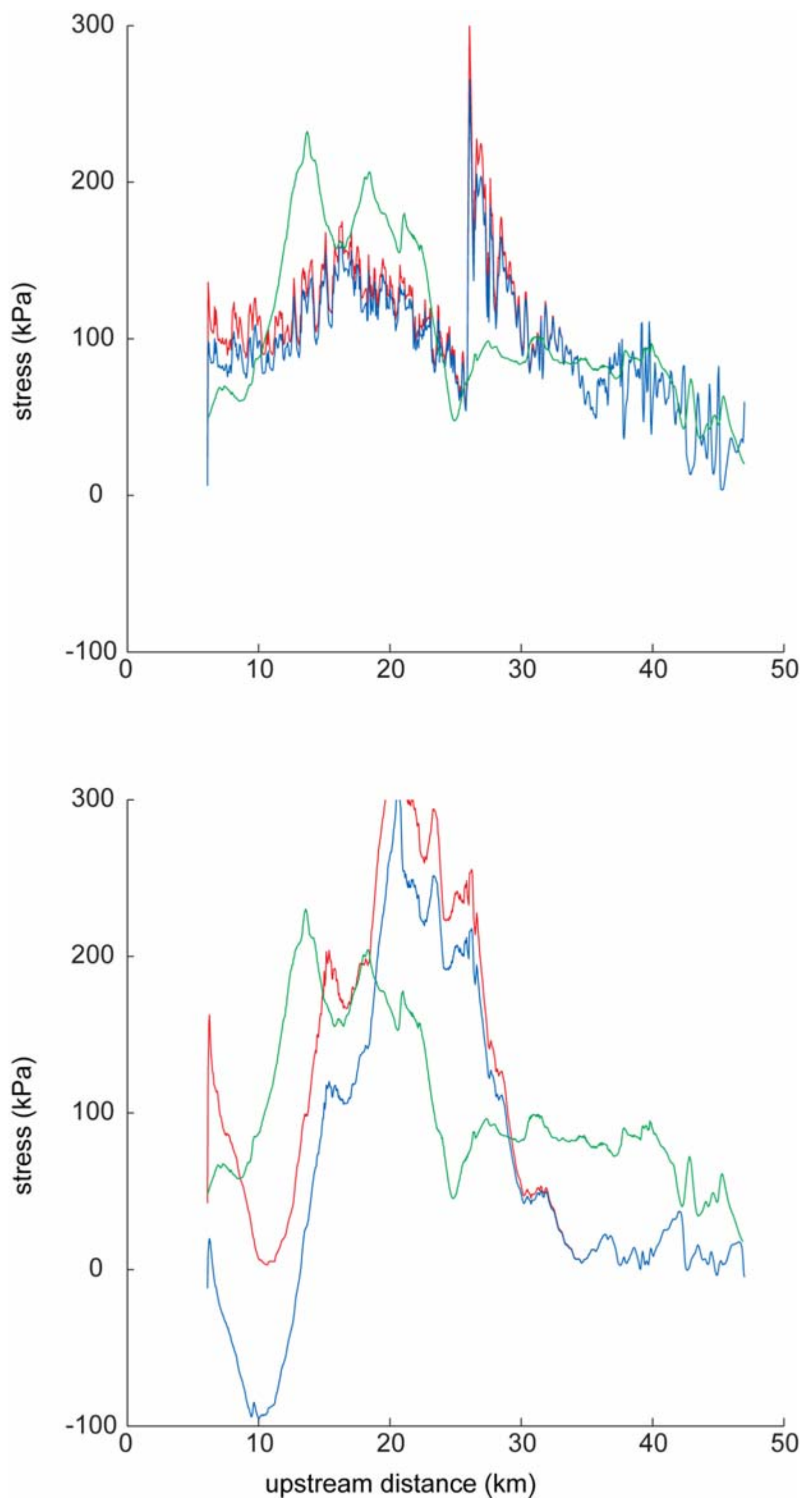

Figure 4.9 Driving stress (green) is compared to the basal shear stress in deformation with sliding model before (blue) and after ice shelf removal (red; upper). Driving stress (green) is compared to the longitudinal stress deformation with sliding model before (blue) and after ice shelf removal (red; lower).

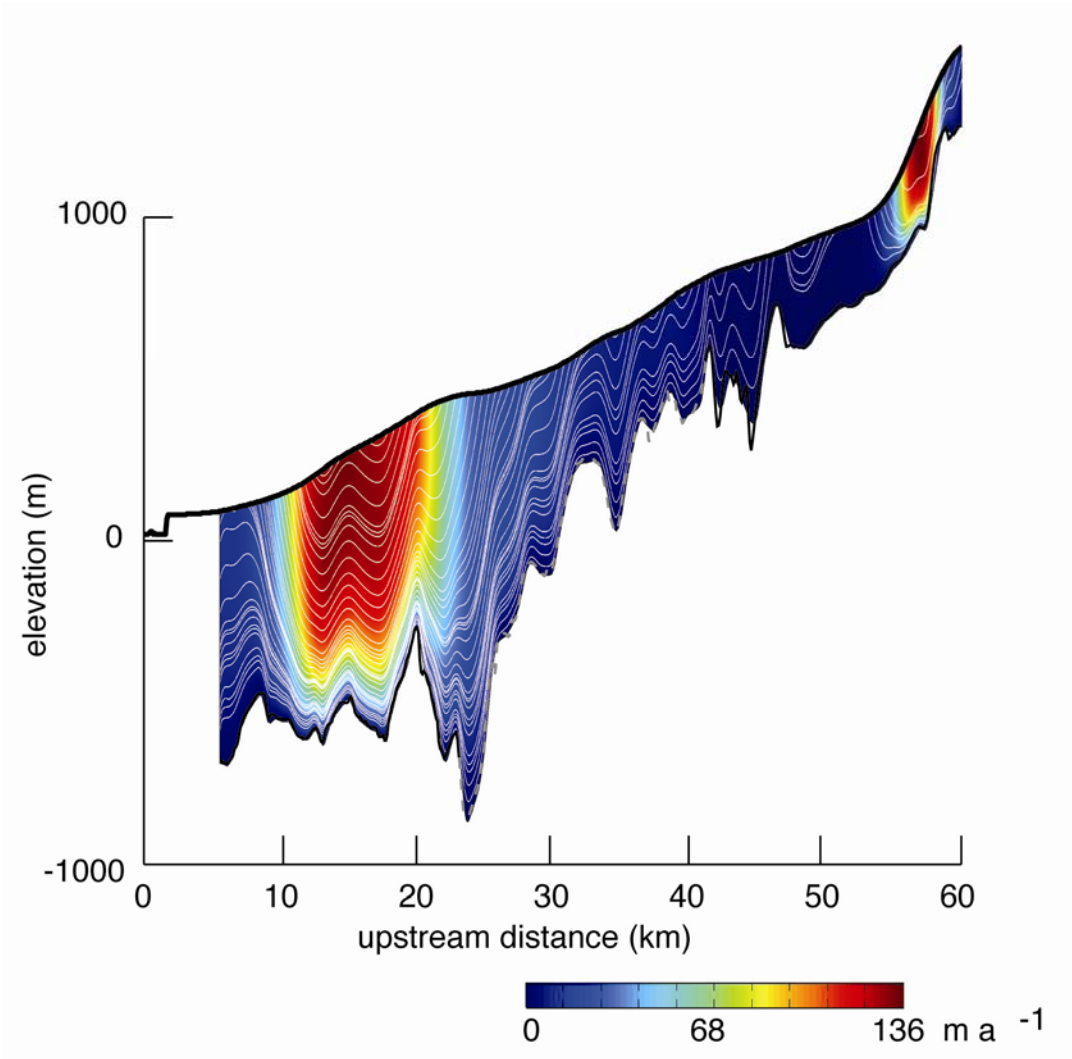

Figure 4.10 Particle paths show ice in the fast flow region from 10 to 20 km upstream and rising at bedrock high at about 9 km upstream.

4.2.2 Effect of ice shelf removal

Ice shelf removal in the deformation only model results a small change in velocity at furthest downstream reach of the glacier (Figure 4.11), indicating the inability of the signal of the stress perturbation to transmit upstream via longitudinal stretching. A significant increase in velocity is seen throughout the downstream reach of the glacier after the ice shelf is removed (Figure 4.12; Figure 4.14 lower).

Response is minimal in the upstream reach of the glacier. Longitudinal stress changes sign in the downstream reach from a compressional to a stretching regime (Figure 4.9; Figure 4.15). Change in shear stress is concentrated downward the downstream end (Figure 4.17).

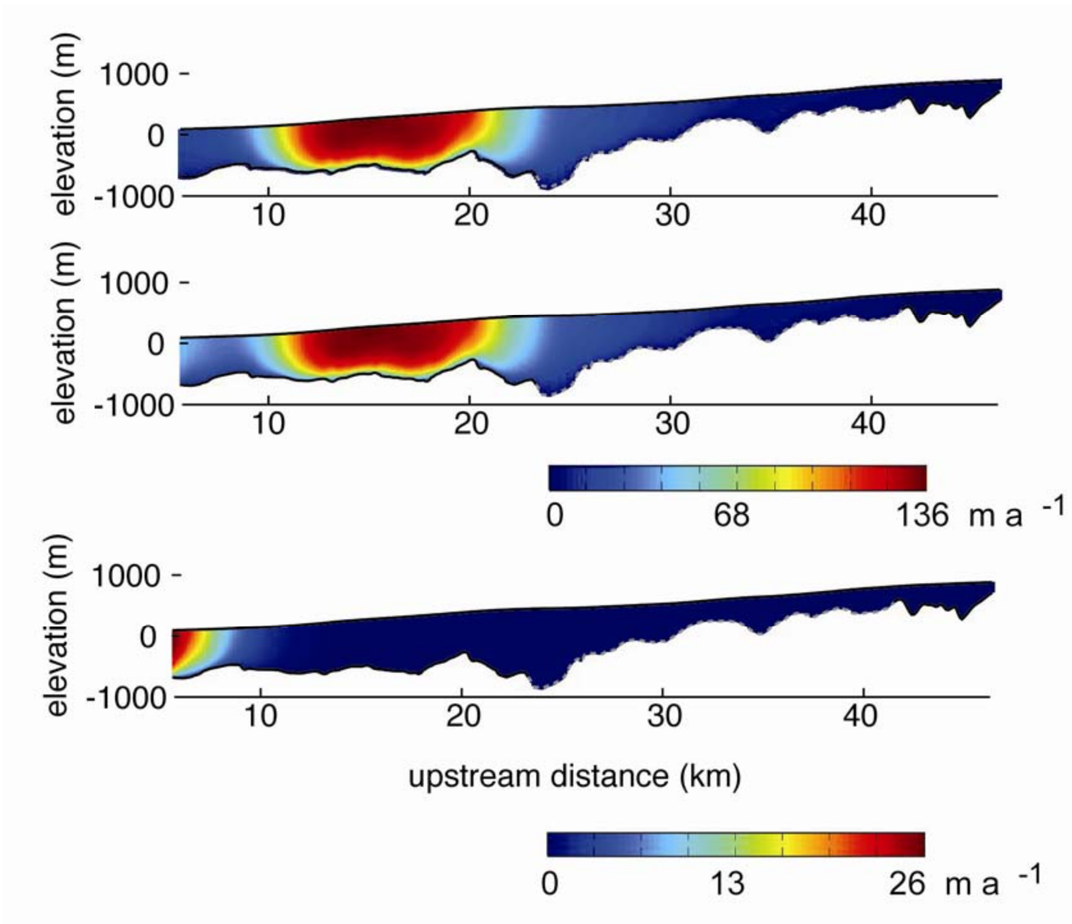

Figure 4.11 Downstream component of velocity vector in models with deformation only is shown, a) prior to ice shelf removal, b) subsequent to ice shelf removal and c) as the difference of the results. Shaded areas represent regions where the basal elevation was recorded from observations.

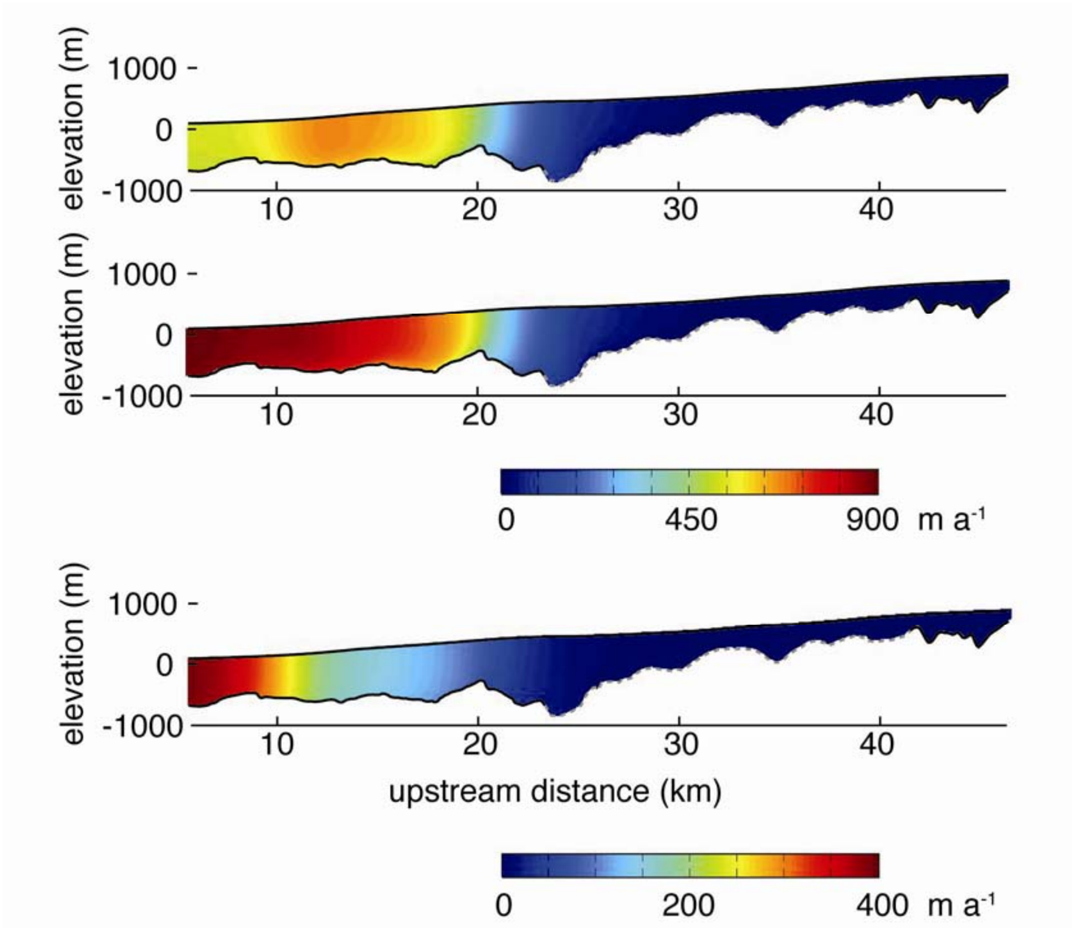

Figure 4.12 Downstream component of velocity vector in models incorporating deformation and sliding is shown prior to ice shelf removal (upper), subsequent to ice shelf removal (middle) and, as the difference of the results (lower). Dashed lines on bed represent regions where the basal elevation was estimated.

The model predicted instantaneous response of surface velocities in the downstream reach closely match observed velocity over the interval 06 Dec. 2001 to 18 Dec. 2002 (Figure 4.14 upper), the time period nearest to ice shelf disintegration. The large speed up response at the downstream reach of the glacier is due to the large sliding parameter *k*.

The instantaneous thinning rate produced by the increase in downstream stretching after ice shelf removal, has an average value of about -14 ma^{-1} in the downstream reach (Figure 4.16). Taking observed change in surface elevation as representative of change in ice thickness, the downstream reach of Crane Glacier thinned about 80 meters near its centerline during its rapid retreat phase from 23 October 2003 to 23 February 2004 (observed via satellite at the ICESat crossover) (Scambos et al., 2004). The model thinning rate is of the correct order of magnitude, compared to observed surface lowering.

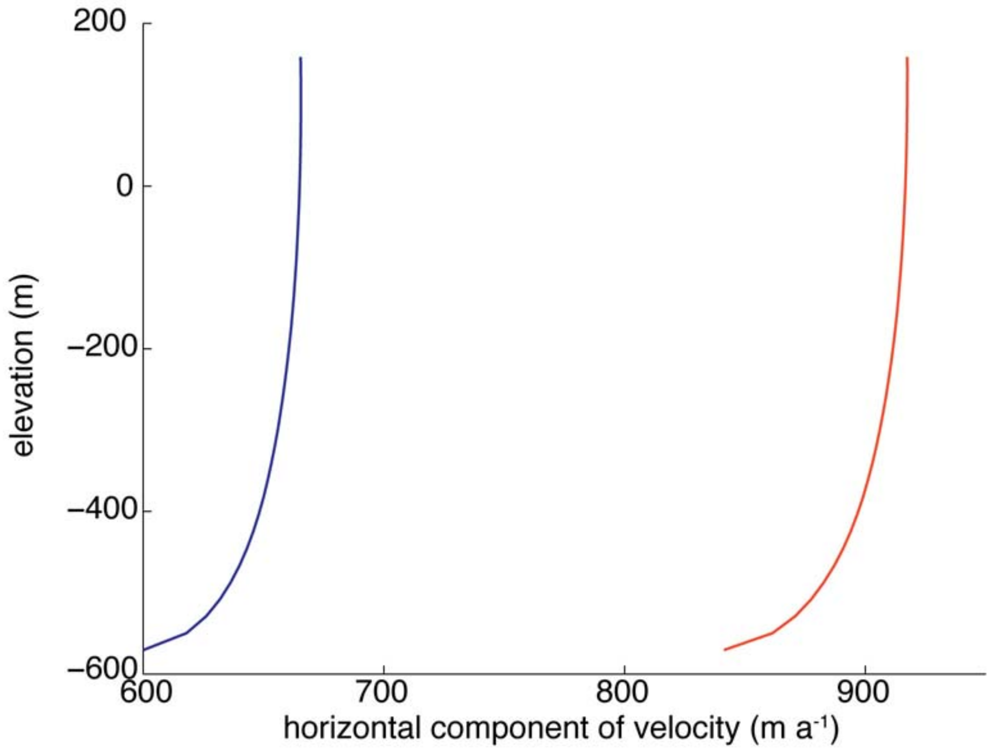

Figure 4.13 Downstream component of velocity is near uniform with depth of a slice 12.5 km upstream both before (blue) and, after (red) ice shelf removal.

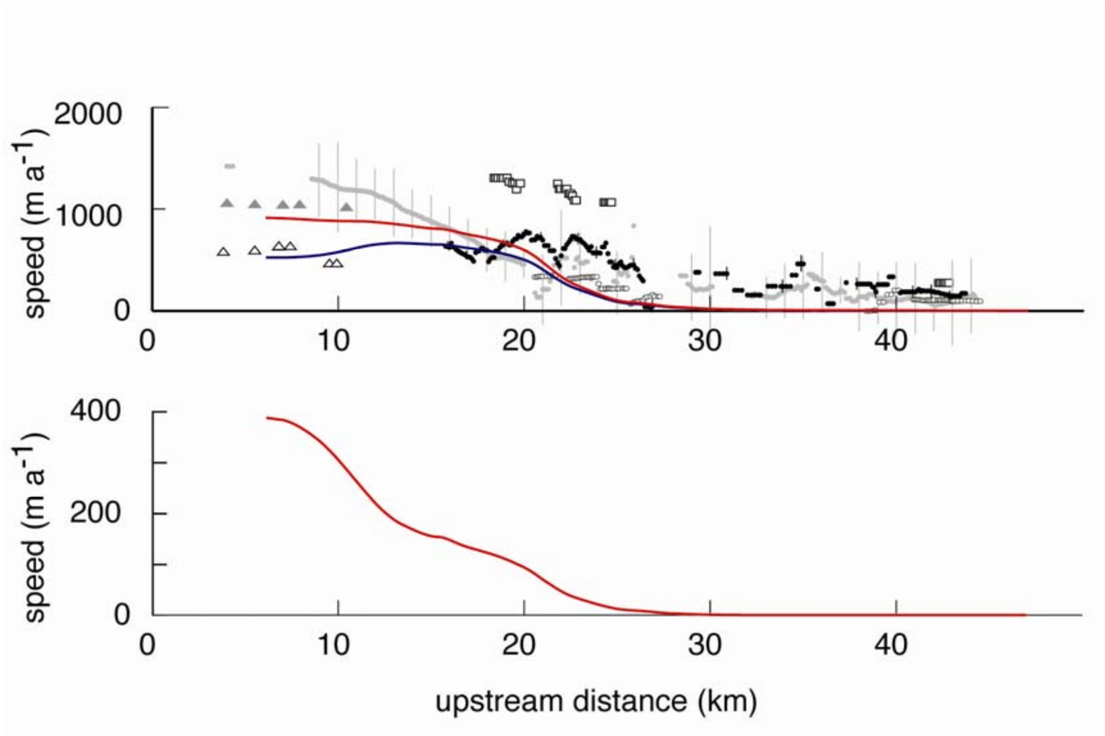

Figure 4.14 The deformation and sliding model predicted horizontal surface velocities prior (blue) and subsequent (red) to ice shelf removal are compared to observations (upper) from 27 January 2000 to 06 December 2001 (hollow triangles), from 06 December 2001 to 18 December 2002 (filled triangles), from 18 December 2002 to 20 February 2003 (filled grey circles), from 18 December 2002 to 13 January 2004 (filled black circles), from 13 January 2004 to 27 September 2004 (hollow circles) and, from 24 November 2005 to 25 November 2006 (hollow squares). The deformation and sliding model surface velocity of the model prior to ice shelf removal is subtracted from the model subsequent to ice shelf removal (lower).

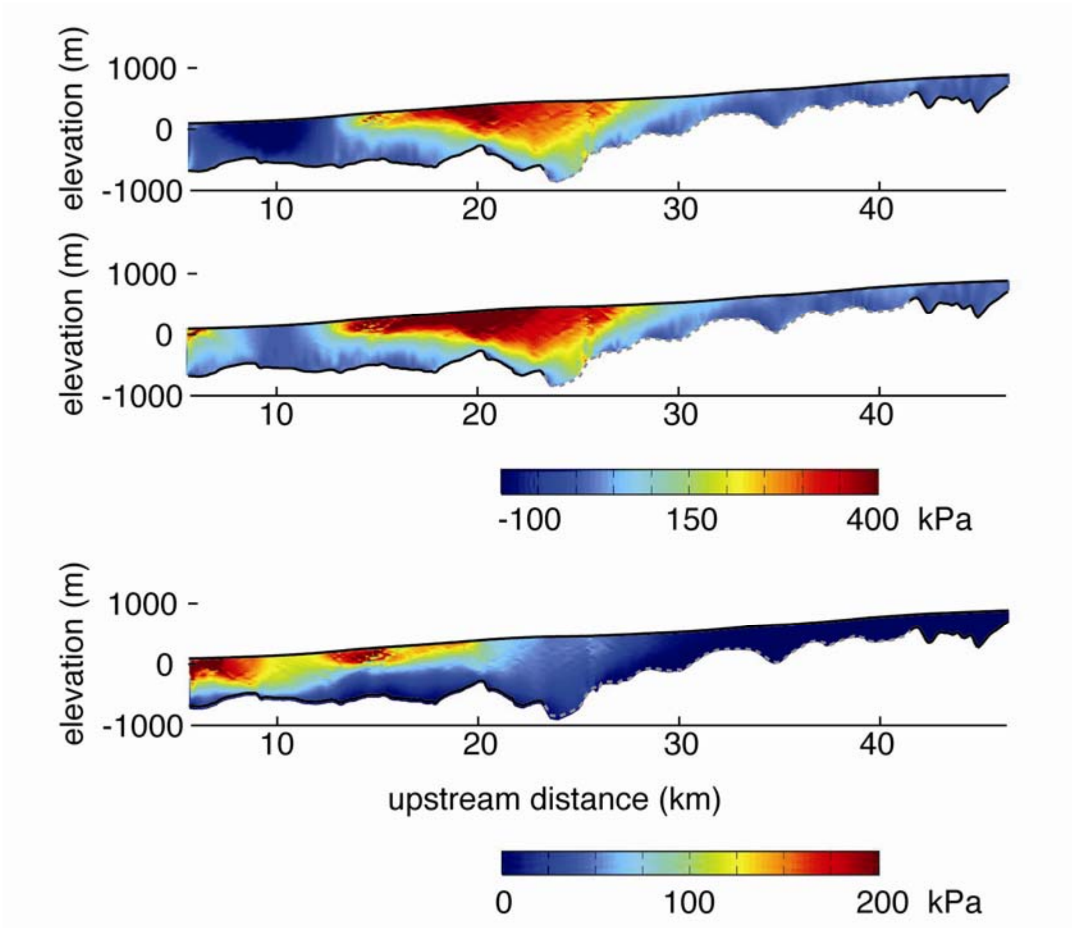

Figure 4.15 Longitudinal component of stress tensor (σ_{xx}) in deformation and sliding model prior to ice shelf removal (upper), subsequent to ice shelf removal (middle) and, as the difference of the results (lower). Dashed lines on bed represent regions where the basal elevation was estimated.

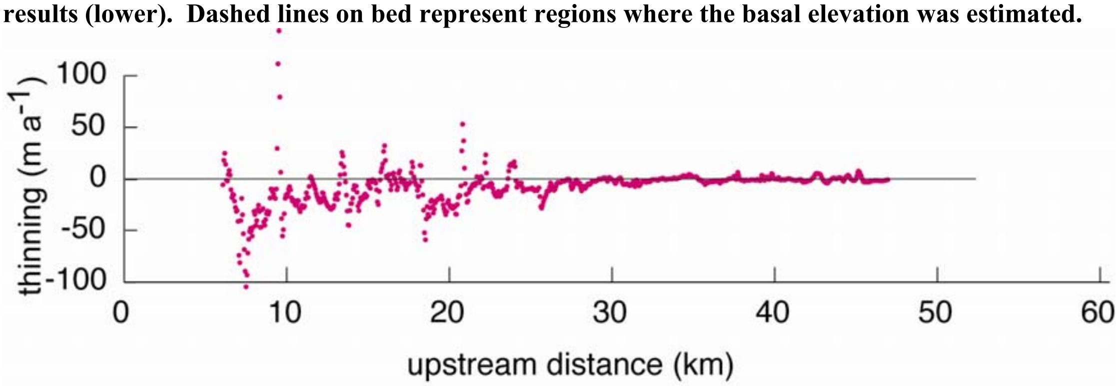

Figure 4.16 The instantaneous thinning rate in response to ice shelf removal.

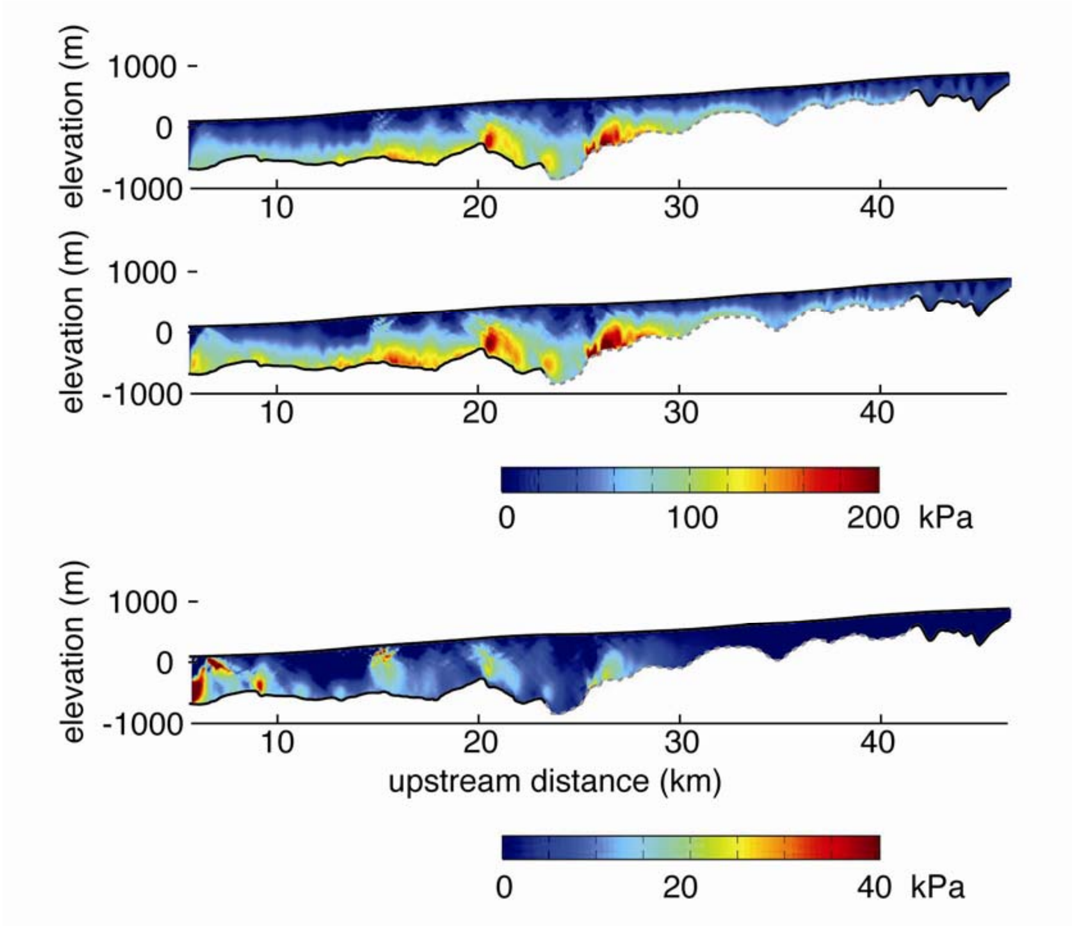

Figure 4.17 Shearing component of stress tensor (σ_{xz}) from deformation and sliding model prior to ice shelf removal (upper), subsequent to ice shelf removal (middle) and, as the difference of the results (lower). Dashed lines on bed represent regions where the basal elevation was estimated.

5 Conclusions and Discussion

The model experiments conducted here may be interpreted to demonstrate that the rapid and large magnitude response of Crane Glacier to collapse of Larsen B ice shelf (Figure 4.12; Figure 4.13) is due to the strong sliding in its downstream reach. In deformation-only model the signal of ice shelf removal does not travel upstream significantly, whereas the signal travels throughout the entire downstream reach the model incorporating sliding (Figure 5.1).The small change in longitudinal stretching due to the change in the downstream stress boundary condition (Figure 4.15) is accompanied by a small change in basal shear stress (Figure 4.17). The large multiplier in the sliding parameterization (tuned to pre-collapse) amplifies the small stress perturbation into a large sliding response.

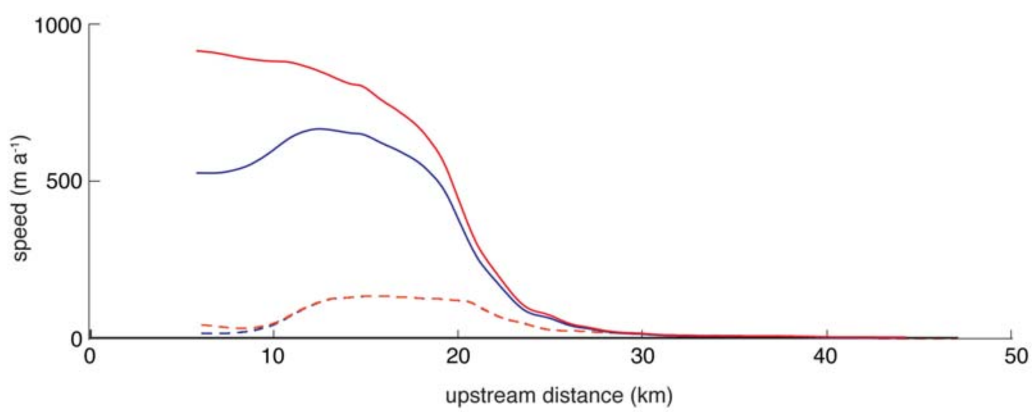

Figure 5.1 Downstream component of surface velocity from deformation only model (dashed) and with sliding (solid) both before (blue) and after (red) ice shelf removal.

The strongest instantaneous response to ice shelf removal, in the model with sliding, occurs downstream of a prominent bedrock high (20 km upstream; Figure 2.2). This feature has an important role in the stress balance within the glacier.

A height above buoyancy relation can be used to locate a stable calving front for a tidewater glacier. A common calving front parameterization (Vieli et al., 2001) assumes that buoyancy of the ice is the controlling factor of ice calving at the downstream end. A critical calving height, h'_c for front stability and is defined as:

$$h_c' = \frac{\rho_w}{\rho}(1+q) \cdot d \tag{5.1}$$

in which, d represents the water depth and q represents a tunable floatation criteria. Ice at the front that is thinner than the local h'_c is assumed to calve away using a standard q value of 0.15, a stable front position is found near where the glacier front stabilized at about 15 km upstream (Figure 2.5).

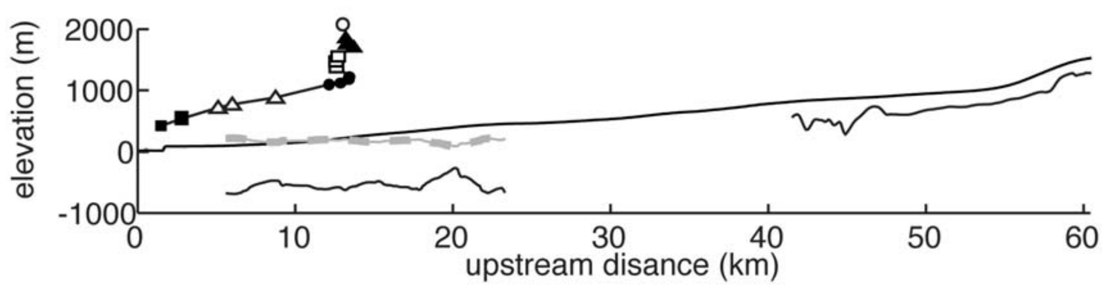

Figure 5.2 Dashed line represents h'_c for given basal elevation and predicted calving stability is shown where line intersects ice surface elevation. Observed front positions are shown for times: summer of 2002-03 (filled squares), summer of 2003-04 (hollow triangles), summer of 2004-05 (filled circles), summer of 2005-06 (hollow squares), summer of 2006-07 (filled triangles) and, summer of 2007-08 (hollow circle).

The observed stable front location from 2005 onward is likely connected to a tidewater calving effect. It is unknown what the coupled effects of calving and glacier speed up are. It is likely that glacier speed up enhances calving retreat, however, moving the front upstream could affect sliding response by modifying the basal water drainage system. It is important to further study the coupled response of this system into to establish the interdependency of these mechanisms.

The tuned value of the multiplier in the sliding parameterization is an order of magnitude larger than values used in other studies. It would thus be of interest to explore this quantity in more detail. One possibility would be to conduct a series of “snapshot” calculations in which the sliding parameters are tuned to different observed velocity fields during glacier retreat. Using ICESat surface elevation data and satellite front position data a thinning rate of the surface elevation of Crane Glacier can be inferred over the entire flightline domain and hence, updated geometry profiles can be constructed for various times. Surface velocity observations can then be used to tune sliding parameters at each time of surface elevation observation.

Changes in tuned sliding parameters with differing geometries can provide indirect evidence of changes in the basal water system. A change in sliding parameters over time would imply a fundamental change in the role of water internal to the glacier and would indicate a strong forcing by a calving mechanism.

6 Works Cited

Bamber, J.L., Riva, R.E.M., Vermeersen, B.L.A., and LeBrocq, A.M., 2009, Reassessment of the Potential Sea-Level Rise from a Collapse of the West Antarctic Ice Sheet: Science, v. 324, p. 901-903.

Benn, D.I., and Evans, D.J.A., 1998, Glacers and Glaciation: London, UK, Arnold, 734 p.

Bindschadler, R., 1983, The importance of pressurized subglacial water in separation and sliding at the glacier bed: Journal of Glaciology, v. 29, p. 3-19.

Björck, Å., 1996, Numerical methods for least squares problems, Society for Industrial Mathematics.

Cook, A., Fox, A., Vaughan, D., and Ferrigno, J., 2005, Retreating glacier fronts on the Antarctic Peninsula over the past half-century: Science, v. 308, p. 541-545.

Davis, T., 2004, A column pre-ordering strategy for the unsymmetric-pattern multifrontal method: AMS Transient Mathematical Softward, v. 30.

Deuflhard, P., 1974, A modified Newton method for the solution of ill-conditioned systems of nonlinear equations with application to multiple shooting.: Numerical Mathematics, v. 22, p. 289-315.

Domack, E., Brachfeld, S., Gilbert, R., Halverson, G., Huber, B., Ishman, S., Leventer, A., Rathburn, A., Rebesco, M., and Willmott, V., 2006, Deep Access To The Larsen Ice Shelf-B Embayment: An International Geologic And Geophysical Expedition (NB Palmer 2006-3).

Glen, J.W., 1955, The creep of polycrystalline ice: Proceedings of the Royal Society of London. Series A, Mathematical and Physical Sciences, p. 519-538.

Hooke, R.L.B., 2005, Principles of Glacier Mechanics: Cambridge, UK, Cambridge University Press, 429 p.

Hulbe, C.L., Scambos, T.A., Youngberg, T., and Lamb, A.K., 2008, Patterns of glacier response to disintegration of the Larsen B ice shelf, Antarctic Peninsula: Global and Planetary Change, v. 63, p. 1-8.

Iken, A., 1981, The effect of the subglacial water pressure on the sliding velocity of a glacier in an idealized numerical model: Journal of Glaciology, v. 27, p. 407-421.

Ingolfsson, O., and Hjort, C., 2002, Glacial history of the Antarctic Peninsula since the Last Glacial Maximum-a synthesis: Polar Research, v. 21, p. 227-234.

Jansson, P., 1995, Water pressure and basal sliding on Storglaciaeren, northern Sweden: Journal of Glaciology, v. 41, p. 232-240.

Johnson, J.V., and Staiger, J.W., 2007, Modeling long-term stability of the Ferrar Glacier, East Antarctica: Implications for interpreting cosmogenic nuclide inheritance: J. Geophys. Res, v. 112.

Kamb, B., Engelhardt, H., Fahnestock, M.A., Humphrey, N., Meier, M., and Stone, D., 1994, Mechanical and hydrologic basis for the rapid motion of a large tidewater glacier 2. Interpretation: J. Geophys. Res, v. 99, p. 15,231–15,244.

Lamb, A.K., 2006, Glacier acceleration after the ice shelf collapse in the Antarctic Peninsula [Senior thesis]: Portland, OR, Portland State University.

Maule, C.F., Purucker, M.E., Olsen, N., and Mosegaard, K., 2005, Heat Flux Anomalies in Antarctica Revealed by Satellite Magnetic Data, Volume 309, American Association for the Advancement of Science, p. 464-467.

Meier, M., Lundstrom, S., Stone, D., Kamb, B., Engelhardt, H., Humphrey, N., Dunlap, W.W., Fahnestock, M., Krimmel, R.M., and Walters, R., 1994, Mechanical and hydrologic basis for the rapid motion of a large tidewater glacier. 1: Observations: Journal of Geophysical Research (ISSN 0148-0227), v. 99.

Morris, E.M., and Vaughan, D.G., 2003, Spatial and temporal variation of surface temperature on the Antarctic Peninsula and the limit of viability of ice shelves: Antarctic Peninsula climate variability: historical and paleoenvironmental perspectives. Washington, DC: American Geophysical Union, Antarctic Research Series, v. 79, p. 61-68.

NSIDC, 2009, IMCORR Software, National Snow and Ice Data Center.

Pattyn, F., 2003, A new three-dimensional higher-order thermomechanical ice sheet model: Basic sensitivity, ice stream, development, and ice flow across subglacial lakes: Journal of Geophysical Research, v. 108, p. 1-15.

Payne, A.J., Vieli, A., Shepherd, A.P., Wingham, D.J., Rignot, E., Casassa, G., Gogineni, P., Krabill, W., Rivera, A., and Thomas, R., 2004, Recent dramatic thinning of largest West Antarctic ice stream triggered by oceans: Geophysical Research Letters, v. 31.

Pritchard, H., 2007, Glaciology of the Antarctic Peninsula, *in* Riffenburgh, B., ed., Encyclopedia of the Antarctic, Routledge.

Rignot, E., Casassa, G., Gogineni, P., Krabill, W., Rivera, A., and Thomas, R., 2004, Accelerated ice discharge from the Antarctica Peninsula following the collapse of the Larsen B ice shelf: Geophysical Research Letters, v. 31.

Scambos, T.A., Bohlander, J.A., Shuman, C.A., and Skvarca, P., 2004, Glacier acceleration and thinning after ice shelf collapse in the Larsen B embayment, Antarctica: Geophysical Research Letters, v. 31.

Scambos, T.A., Hulbe, C., and Fahnestock, M., 2003, Climate-Induced ice shelf disintegration in the Antarctic Peninsula, Antarctic Research Series: Antarctic Peninsula Climate Variability, American Geophysical Union, p. 79-92.

Scambos, T.A., Hulbe, C., Fahnestock, M., and Bohlander, J., 2000, The link between climate warming and break-up of ice shelves in the Antarctic Peninsula: Journal of Glaciology, v. 46, p. 516-530.

Shuman, C.A., Scambos, T.A., Krabill, W., Thomas, R., Martin, C., Casassa, G., Rivera, A., and Hulbe, C., 2008, Dynamic glacier thinning in the Larsen B embayment, Antartica, 2002-2007, International symposium on dynamics in glaciology.: Limerick, Ireland.

Steig, E.J., Schneider, D.P., Rutherford, S.D., Mann, M.E., Comiso, J.C., and Shindell, D.T., 2009, Warming of the Antarctic ice-sheet surface since the 1957 International Geophysical Year: Nature, v. 457, p. 459-462.

Thomas, R., 2005, Personal Communication.

Thomas, R., Rignot, E., Casassa, G., Kanagaratnam, P., Acuna, C., Akins, T., Brecher, H., Frederick, E., Gogineni, P., Krabill, W., Manizade, S., Ramamoorthy, H., Rivera, A., Russell, R., Sonntag, J., Swift, R., Yungel, J., and Zwally, J., 2004, Accelerated Sea-Level Rise from West Antarctica: Science, v. 306, p. 255-258.

Van der Veen, C.J., 1999, Fundamentals of Glacier Dynamics: Rotterdam, Netherlands, A.A. Balkema, 462 p.

van Lipzig, N.P.M., King, J.C., Lachlan-Cope, T.A., and van den Broeke, M.R., 2004, Precipitation, sublimation, and snow drift in the Antarctic Peninsula region from a regional atmospheric model: J. Geophys. Res, v. 109.

Vaughan, D.G., and Doake, C.S.M., 1996, Recent atmospheric warming and retreat of ice shelves on the Antarctic Peninsula: Nature, v. 379, p. 328-331.

Vieli, A., Funk, M., and Blatter, H., 2000, Tidewater glaciers: frontal flow acceleration and basal sliding: Annals of Glaciology, v. 31, p. 217-221.

—, 2001, Flow dynamics of tidewater glaciers: a numerical modelling approach: Journal of Glaciology, v. 47, p. 595-606.

Zwally, H.J., Schutz, B., Abdalati, W., Abshire, J., Bentley, C., Brenner, A., Bufton, J., Dezio, J., Hancock, D., and Harding, D., 2002, ICESat's laser measurements of polar ice, atmosphere, ocean, and land: Journal of Geodynamics, v. 34, p. 405-445.